

Simulation of Late Summer Arctic Clouds during ASCOS with Polar WRF

KEITH M. HINES AND DAVID H. BROMWICH

Polar Meteorology Group, Byrd Polar and Climate Research Center, The Ohio State University, Columbus, Ohio

(Manuscript received 2 March 2016, in final form 27 September 2016)

ABSTRACT

Low-level clouds are extensive in the Arctic and contribute to inadequately understood feedbacks within the changing regional climate. The simulation of low-level clouds, including mixed-phase clouds, over the Arctic Ocean during summer and autumn remains a challenge for both real-time weather forecasts and climate models. Here, improved cloud representations are sought with high-resolution mesoscale simulations of the August–September 2008 Arctic Summer Cloud Ocean Study (ASCOS) with the latest polar-optimized version (3.7.1) of the Weather Research and Forecasting (Polar WRF) Model with the advanced two-moment Morrison microphysics scheme. Simulations across several synoptic regimes for 10 August–3 September 2008 are performed with three domains including an outer domain at 27-km grid spacing and nested domains at 9- and 3-km spacing. These are realistic horizontal grid spacings for common mesoscale applications. The control simulation produces excessive cloud liquid water in low clouds resulting in a large deficit in modeled incident shortwave radiation at the surface. Incident longwave radiation is less sensitive. A change in the sea ice albedo toward the larger observed values during ASCOS resulted in somewhat more realistic simulations. More importantly, sensitivity tests show that a reduction in specified liquid cloud droplet number to very pristine conditions increases liquid precipitation, greatly reduces the excess in simulated low-level cloud liquid water, and improves the simulated incident shortwave and longwave radiation at the surface.

1. Introduction

The Arctic region is especially sensitive to climate change as it is warming twice as fast as the global average with the largest changes near the surface (Serreze and Francis 2006; Serreze et al. 2009; Jeffries and Richter-Menge 2015). Clouds, which impact the surface energy balance by reflecting shortwave radiation and absorbing and emitting longwave radiation, are extensive over the Arctic Ocean, yet the regional climate processes involving clouds are inadequately understood (Vavrus 2004; Verlinde et al. 2007; Tjernström et al. 2008; Eastman and Warren 2010; Hwang et al. 2011; Shupe et al. 2015). Seasonal cloud fractions peak in late summer or early autumn near 85% coverage (Intrieri et al. 2002; Tjernström et al. 2008; Karlsson and Svensson 2011). Arctic cloud cover is especially manifested in persistent low clouds (Curry et al. 1996; Intrieri et al. 2002; Eastman and Warren 2010; Shupe et al. 2015).

Moreover, the relationship between stratus clouds and low-level static stability at lower latitudes does not hold in the Arctic. At lower latitudes, the season of highest cloud amount matches the highest static stability, but in the Arctic higher cloud fractions are observed in the lower static stability summer (Klein and Hartmann 1993).

While the ice–albedo feedback is an obvious driver of climate change, clouds are also important to Arctic feedbacks, albeit in ways less well understood (Intrieri et al. 2002; Francis and Hunter 2006; Francis et al. 2009; Graversen and Wang 2009). Vavrus (2004) found the climate change impact to be particularly large in a CO₂ modeling study with about 40% of Arctic warming from cloud modulation. Other studies find that clouds are important contributors to sea ice processes (Ebert and Curry 1993; Francis and Hunter 2006; Eastman and Warren 2010; Karlsson and Svensson 2011). Conversely, sea ice modulates Arctic clouds (Kay et al. 2008; Eastman and Warren 2010). Vavrus et al. (2011) find that the diminishing sea ice coverage should increase cloudiness in the Arctic. Therefore, studies of both the observed large sea ice loss in recent decades and the projected even larger changes over the twenty-first century must consider the role of clouds within climate change.

Byrd Polar and Climate Research Center Contribution Number 1548.

Corresponding author e-mail: Keith M. Hines, hines@polarmet1.mps.ohio-state.edu

DOI: 10.1175/MWR-D-16-0079.1

For both present-day numerical forecasts and simulations of future climate, models must apply parameterizations of clouds given the large-scale differences between climate model resolution, individual cloud structure, and the base microphysics processes. Some studies use sufficient resolution to resolve microscale features of cloud systems with horizontal grid spacings of 1 km or less (e.g., Klein et al. 2009; Morrison et al. 2009; Solomon et al. 2015). Computational considerations, however, for many mesoscale studies result in the use of coarser resolutions. Our interests reside in the representation of polar clouds for simulations at these coarser resolutions. The demands upon cloud parameterization may be especially large during the transition from late summer to early autumn, including the sea ice minimum and the freeze-up that follows (e.g., Kay and Gettelman 2009; Sedlar et al. 2011), as large-scale models cannot resolve the local low-level thermodynamic interaction between sea ice, atmospheric stability, and clouds (e.g., Karlsson and Svensson 2011; Barton et al. 2012). However, successfully representing polar clouds in numerical atmospheric models has proven to be a challenge (e.g., Luo et al. 2008; Tjernström et al. 2008; Vavrus et al. 2009; Klein et al. 2009; Barton et al. 2012; Birch et al. 2012; de Boer et al. 2012; Wesslén et al. 2014). For example, some studies have found that climate models such as the fifth version of the Community Atmosphere Model (CAM5) and the Laboratoire de Météorologie Dynamique model with zoom capacity tend to underpredict the formation of optically thin liquid clouds with supercooled water (e.g., Cesana et al. 2012). Vavrus et al. (2009) show large differences in the seasonal cloud fraction between Coupled Model Intercomparison Project phase 3 (CMIP3) models. Arctic mixed-phase clouds with the interactive physics of both liquid water and ice are a particular challenge (e.g., Morrison et al. 2012; Solomon et al. 2015; Sotiropoulou et al. 2016). Consequently, uncertainty in cloud simulations contributes to climate models showing greater variability in the forecasted future temperature in Arctic latitudes than at lower latitudes (Chapman and Walsh 2007). Low-level clouds especially contribute to model uncertainty (Williams and Webb 2009).

Multiple observational programs within the past two decades have sought to address the Arctic cloud challenges (e.g., Uttal et al. 2002; Verlinde et al. 2007; McFarquhar et al. 2011; Tjernström et al. 2014; Smith et al. 2017). Efforts continue to implement more advanced cloud representations within models (Morrison et al. 2005; Luo et al. 2008; Morrison and Gettelman 2008; Gettelman et al. 2010; Lim and Hong 2010; Liu et al. 2012; English et al. 2014; Forbes and Ahlgrim

2014; Park et al. 2014; Thompson and Eidhammer 2014). While these efforts are not necessarily all targeted for polar clouds, it is hoped that improved physics will ultimately produce better representations of regional characteristics. Yet, existing schemes are still not sufficiently tested against Arctic data, and many cloud schemes are developed based upon observations of mid-latitude and tropical cloud properties (Randall et al. 1998; Tjernström et al. 2014). Many remaining gaps are related to predicting the phase of cloud and precipitation particles, given that supercooled water is common at higher latitudes.

Here, we evaluate the polar-optimized version of the Weather Research and Forecasting (WRF) Model (Skamarock et al. 2008), known as Polar WRF (PWRf), for simulations of clouds over the high Arctic during the Arctic Summer Cloud Ocean Study (ASCOS) that encompassed the transition, including surface freeze-up, from late summer to early autumn. Section 2 describes the ASCOS study and the observational data used for comparison with model output. Section 3 describes Polar WRF and the model setup. Section 4 displays model output for a control simulation. Section 5 discusses sensitivity experiments. Conclusions are presented in section 6.

2. ASCOS

The Arctic Summer Cloud Ocean Study (Tjernström et al. 2014) is an international Arctic observational study that took place during August and September 2008 that featured the Swedish icebreaker *Oden* drifting for 3 weeks with a 3 km × 6 km ice floe north of 87°N and between 1° and 11°W (Fig. 1). ASCOS studied physical and chemical processes leading to cloud formation, with goals of better understanding life cycles of summer low-level clouds in the high Arctic and better simulations of Arctic clouds in climate models. Occasionally, limited cloud condensation nuclei (CCN), with concentrations sometimes less than 1 cm⁻³, inhibited low-level cloud formation and were associated with the tenuous cloud regime studied by Mauritsen et al. (2011). ASCOS, which ran through the latter part of the melt season into autumn freeze-up, included detailed measurements of the surface energy balance. Meteorological conditions during the project are described by Tjernström et al. (2012).

Sedlar et al. (2011) divided the ASCOS period from 13 August to 1 September into four regimes based upon temperature and cloud structure. The first and third regimes at ASCOS were relatively warm and had extensive low clouds. The other two had fewer low clouds and were denoted by observed air temperatures well

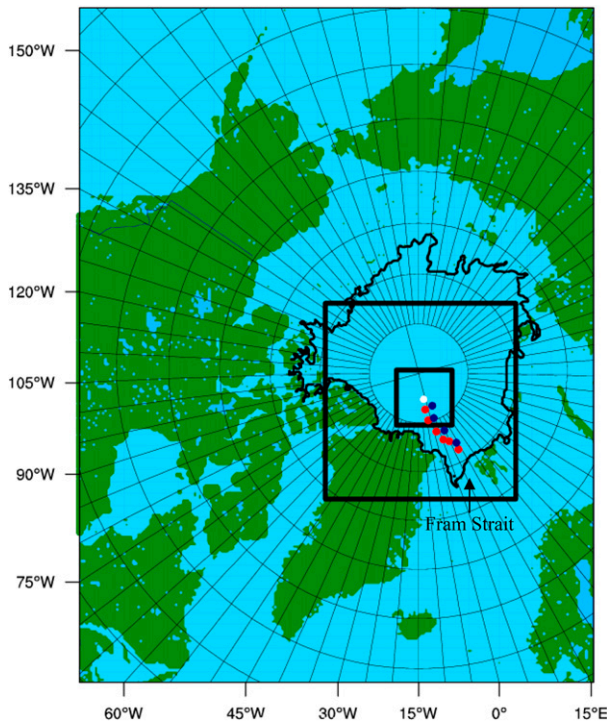


FIG. 1. Map of the Arctic domain showing the 27-, 9-, and 3-km horizontal grid-spacing domains. The 0000 UTC positions for the *Oden* for 6–11 Aug 2008 are shown by the red dots. The blue dots show the positions for 3–6 Sep. The average location of the icebreaker *Oden* for regimes 1–4 (see text) is shown by the white dot. The region within the thick black curve has sea ice concentration greater than 0.5 on 25 Aug 2008.

below freezing. Birch et al. (2012), Tjernström et al. (2012), and Sotiropoulou et al. (2014) later subdivided Sedlar et al.'s regime 1, denoted by occasional deep frontal clouds, into an early stage that was more synoptically active and had greater temperature variability and a less active second stage. These defined regimes provide convenient, albeit short term, study periods that we can use for the modeling study.

The detailed observations from ASCOS are discussed in several articles (Mauritsen et al. 2011; Sedlar et al. 2011; Tjernström et al. 2012, 2014; Shupe et al. 2013; de Boer et al. 2014; Sotiropoulou et al. 2014); therefore, only a brief review is given here. Many of the ASCOS observations were gathered from shipborne sensors (Sedlar et al. 2011; Tjernström et al. 2014). Other observations were obtained from ice-deployed instruments. An onboard automatic weather station took continuous observations of basic meteorological quantities. Rawinsondes were launched every 6 h from early 3 August through 7 September (Sedlar et al. 2011, 2012; Tjernström et al. 2014). Cloud quantities including vertical boundaries are obtained from a vertically pointing 35-GHz Doppler Millimeter Cloud Radar (MMCR) combined

with a laser ceilometer. Cloud liquid water path (LWP) was derived from microwave radiometer measurements at 23 and 30 GHz (Shupe et al. 2013). The uncertainty for observed LWP is approximately 25 g m^{-2} (Westwater et al. 2001), which Shupe et al. (2013) note is relatively large compared to frequent observed amounts under 50 g m^{-2} . Ice water path (IWP) is estimated from a combination of different sensors, including the MMCR. Ice water content (IWC) is obtained from radar reflectivity using the formula of Shupe et al. (2005, 2013). The uncertainty of IWC is perhaps a factor of 2 (Shupe et al. 2005). Therefore, these observed quantities can be used for rough guidance in model comparisons. Precision solar pyranometers and precision infrared radiometers observed shortwave and longwave radiation, respectively, on the ice floe. The uncertainty of incident shortwave radiation is about 3 W m^{-2} , and the uncertainty of the longwave measurements is about 4 W m^{-2} (Sedlar et al. 2011). Radiation measurements were initially impacted by two 30-m melt ponds that eventually froze and were then covered by snow and rime accumulation (Sedlar et al. 2011). Turbulent flux estimates of sensible and latent heat are derived from two techniques (O. Persson 2016, personal communication). Sensible heat fluxes are obtained from covariance fluxes from the tower on the ice floe. Latent heat fluxes are taken from a bulk method, with the Marine Atmosphere Emitted Radiance Interferometer (MAERI) radiometer on the *Oden* providing surface and air temperature data. Wind and humidity measurements are from the ship's weather station. The cloud radiative forcing of Sedlar et al. (2011) was obtained from surface radiative flux observations and clear-sky radiative fluxes from a delta-four-stream approximation, correlated- k radiative transfer model.

3. Polar WRF

We present simulations with the polar-optimized version of WRF version 3.7.1 (V3.7.1) known as Polar WRF (<http://polarmet.osu.edu/PWRF/>). Polar optimizations are included in the Noah LSM (Barlage et al. 2010) and improve the representation of heat transfer through snow and ice (Hines and Bromwich 2008; Hines et al. 2015). Fractional sea ice was implemented in Polar WRF by Bromwich et al. (2009) and this was followed by the addition of specified variable sea ice thickness, snow depth on sea ice, and sea ice albedo. These updated options were developed by the Polar Meteorology Group (PMG) at Ohio State University's Byrd Polar and Climate Research Center and were ultimately included in the standard release of WRF (<http://www.wrf-model.org/index.php>) with the help of the Mesoscale

and Microscale Meteorology Division at NCAR (Hines et al. 2015). For the simulations presented here the fractional sea ice concentration and sea ice thickness at 6.25-km spacing are processed by the University of Illinois at Urbana–Champaign from Advanced Microwave Scanning Radiometer for Earth Observing System (AMSR-E) observations (Lobl 2001). Snow depth on sea ice is from Pan-Arctic Ice-Ocean Modeling and Assimilation system (PIOMAS) analysis (Lindsay et al. 2009; Hines et al. 2015). Sea ice albedo follows the seasonal Arctic formula of Wilson et al. (2011), unless otherwise specified. Gridded fields of sea ice concentration, thickness, and albedo, along with snow depth on sea ice during ASCOS, are available for input into WRF runs online (<http://polarmet.osu.edu/hines/PWRF/>).

Polar WRF has been tested over permanent ice (Hines and Bromwich 2008; Bromwich et al. 2013), Arctic pack ice (Bromwich et al. 2009; Hines et al. 2015), and Arctic land (Hines et al. 2011; Wilson et al. 2011, 2012). The model has been applied to various polar applications including Antarctic real-time weather forecasts (e.g., Powers et al. 2012). Hines et al. (2011) made comparisons for cloud and radiation quantities between Polar WRF 3.0.1.1 simulations and observations near the North Slope of the Alaska Atmospheric Radiation Measurement site. Over a nearby Arctic Ocean grid point, Hines et al. (2011) found that the Morrison microphysics scheme produced reasonable shortwave and longwave radiation results in comparison to summer observations at Barrow, Alaska, although much larger radiation biases were found over land (see their Fig. 11). The simulated monthly precipitation and cloud fraction, along with impacted longwave and shortwave biases, over Arctic land were examined by Wilson et al. (2012). More recently, Hines et al. (2015) did some comparisons between winter simulation results and surface radiation measurements from the Surface Heat Budget of the Arctic (SHEBA; Uttal et al. 2002) observations in 1998. Previously, a preliminary release of the Arctic System Reanalysis (ASR) was tested against ASCOS observations (Wesslén et al. 2014). That early version of the ASR used the relatively simple WRF single-moment, 5-class microphysics scheme that is known to underrepresent liquid water in polar clouds. Otherwise, detailed comparisons between Polar WRF simulations and detailed summer cloud observations over the high Arctic have not previously been performed.

The choice of physical parameterizations for simulations described here is based upon the previous history of Polar WRF usage (e.g., Wilson et al. 2011, 2012; Bromwich et al. 2013; Steinhoff et al. 2013). The two-moment Morrison scheme (Morrison et al. 2005, 2009) is applied for cloud microphysics. This bulk

microphysics scheme predicts mixing ratios for cloud water, cloud ice, rain, snow, and graupel. Number concentrations are also predicted for cloud ice, snow, rain, and graupel. The liquid water droplet concentration, however, is specified in the WRF implementation. The Morrison scheme is most frequently used with Polar WRF (e.g., Hines et al. 2011, 2015).

For other parameterization selections, the Mellor–Yamada–Nakanishi–Niino (MYNN; Nakanishi and Niino 2006) level-2.5 scheme is used for the atmospheric boundary layer and the corresponding atmospheric surface layer. We use the climate model–ready update to the Rapid Radiative Transfer Model known as RRTMG (Clough et al. 2005) for longwave and shortwave radiation, as recent testing indicates improved radiative fields. The two-stream treatment of shortwave radiation can treat multiple reflections between cloud and the ice surface. Cloud liquid water, cloud ice, and snow impact the shortwave and longwave radiation, but rainwater is not used in the radiation calculations. In the vertical 57 layers are used, with a top at 10 hPa. Ten levels are in the lowest kilometer of the atmosphere, with the lowest two levels near 8 and 30 m above the surface.

As to the adequacy of the vertical resolution employed here, McInnes and Curry (1995) suggest that the optimum vertical grid spacing for the simulation of summertime Arctic clouds is 25 m for the lowest 2 km of the atmosphere. When they degraded the vertical spacing to 200 m, the model still captured the broad qualitative features for the observed boundary layer. In cloud-resolving simulations with WRF Solomon et al. (2014) found the cloud-layer structure to be insensitive to changes in vertical resolution. Birch et al. (2012) also found limited sensitivity to vertical resolution in ASCOS simulations with a single-column model. When they reduced both the vertical and horizontal spacing by a factor of 2, the result was an increase in the liquid water path by 5% and ice water path by 1%. A test of the impact of vertical resolution in the present Polar WRF simulations of ASCOS indicated that a doubling of the number of layers in the lowest 1.5 km of the troposphere produces small changes in most state variables and surface radiation fluxes. There was a 7.1% increase in liquid water path with the reduced vertical spacing.

The three-domain grid with two-way nesting is shown in Fig. 1. The outer domain is 220×280 and has 27-km grid spacing. The middle domain is 250×250 and has 9-km spacing. The high-resolution inner domain is 202×202 and has 3-km spacing. The Grell-3 cumulus parameterization is applied to the outer two grids, with no cumulus parameterization on the 3-km

TABLE 1. List of numerical simulations.

Simulation	Sea ice albedo	Cloud microphysics
Control	Standard PWRf	Standard two-moment Morrison scheme with 250 cm^{-3} liquid cloud droplet concentration specified
Snow Albedo	New snow-depth formula	Standard two-moment Morrison scheme with 250 cm^{-3} liquid cloud droplet concentration specified
Morrison 100 cm^{-3}	New snow-depth formula	Two-moment Morrison scheme with 100 cm^{-3} liquid cloud droplet concentration specified
Morrison 50 cm^{-3}	New snow-depth formula	Two-moment Morrison scheme with 50 cm^{-3} liquid cloud droplet concentration specified
Morrison 20 cm^{-3}	New snow-depth formula	Two-moment Morrison scheme with 20 cm^{-3} liquid cloud droplet concentration specified
Morrison 10 cm^{-3}	New snow-depth formula	Two-moment Morrison scheme with 10 cm^{-3} liquid cloud droplet concentration specified
Morrison 1 cm^{-3}	New snow-depth formula	Two-moment Morrison scheme with 1 cm^{-3} liquid cloud droplet concentration specified

grid. The innermost grid has insufficient resolution to represent the microscale (scale of about 1 km or less); however, our interest is in the representation of Arctic clouds with commonly used mesoscale grid spacings.

The model is run in forecast mode with a series of 48-h segments initialized daily at 0000 UTC beginning on 9 August 2008. We select 24-h spinup of the clouds, precipitation, and the boundary layer similar to Hines et al. (2011, 2015) and Wilson et al. (2011) to provide a firm test and ensure adequate adjustment. Accordingly, near-surface values will adjust to the model’s surface energy balance and may differ from the initial conditions. Hourly output at 24–47 h is concatenated into a dataset

spanning from 0000 UTC 10 August to 2300 UTC 3 September, approximately that period when the *Oden* was north of 85°N and inside the 3-km domain (Fig. 1). Initial and boundary conditions of basic meteorological fields are interpolated from ERA-Interim (ERA-I; Dee et al. 2011) fields available every 6 h across 32 pressure levels and the surface at T255 resolution. Spectral nudging on the coarse domain is included in our simulations as our emphasis is on the simulation of clouds, not the simulation of the synoptic-scale pattern. Spectral nudging is effective at reducing the gradual drift toward unrealistic flow patterns over the Arctic (Cassano et al. 2011; Glisan et al. 2013;

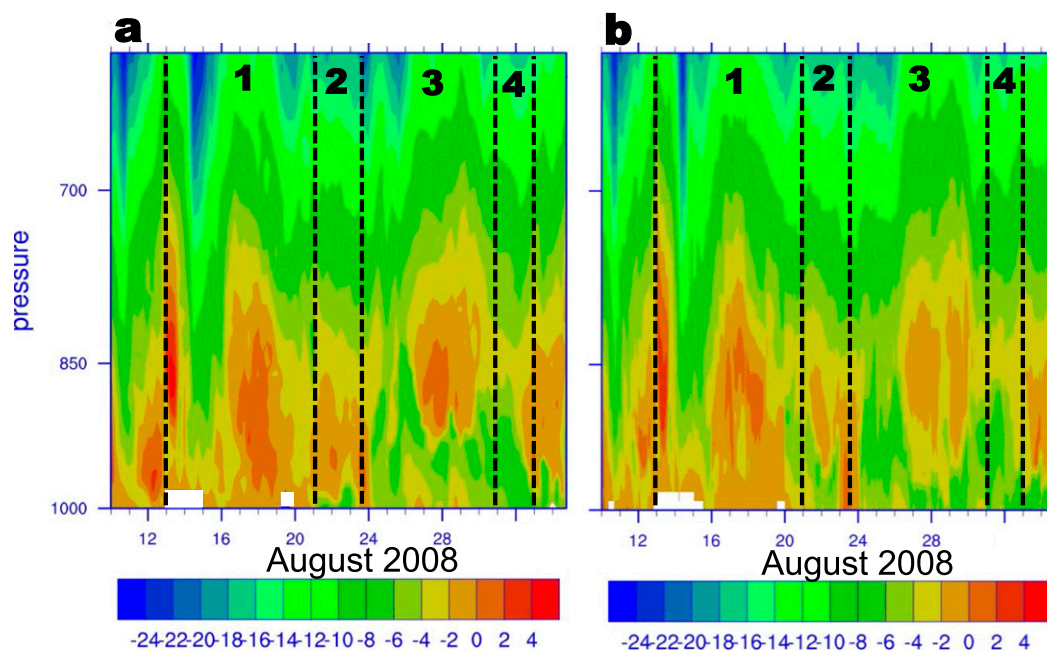


FIG. 2. Vertical profiles of temperature ($^\circ\text{C}$) as a function of days after 31 Jul 2008 for the (a) ASCOS radiosonde observations and (b) PWRf Control simulation. The dashed lines separate the four regimes of ASCOS.

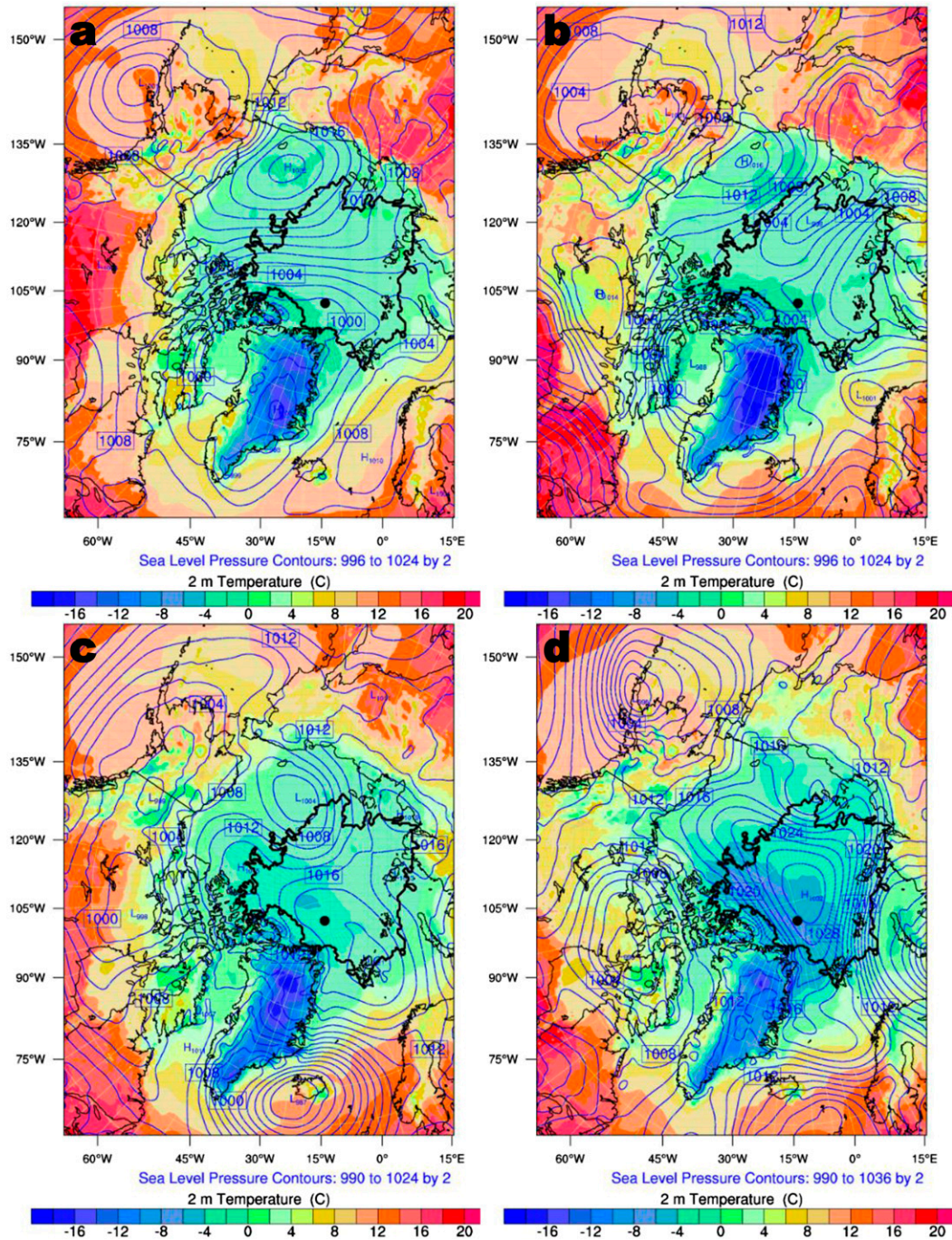


FIG. 3. Simulated mean sea level pressure (hPa) and 2-m temperature ($^{\circ}\text{C}$) for the Control simulation averaged over (a) regime 1 during 13–20 Aug, (b) regime 2 during 21–23 Aug, (c) regime 3 during 23–30 Aug, and (d) regime 4 during 31 Aug–1 Sep. Contour interval is 2 hPa. The area within the thick black contour had sea ice concentrations greater than 0.5 on 25 Aug 2008. The dot is the mean location of the *Oden* during regimes 1–4.

Hines et al. 2015). The spectral nudging is set for truncation at wavenumber 4 in both horizontal directions for model levels above level 10. Thus, only the larger-scale synoptic conditions (wavelengths > 1150 km) are nudged. The nudging coefficients for the temperature, geopotential

height, and horizontal wind components are set at 0.0003 s^{-1} , which represents approximately 56 min in relaxation time. A sensitivity test conducted for regime 3 indicated that spectral nudging had a small impact on the simulated fields.

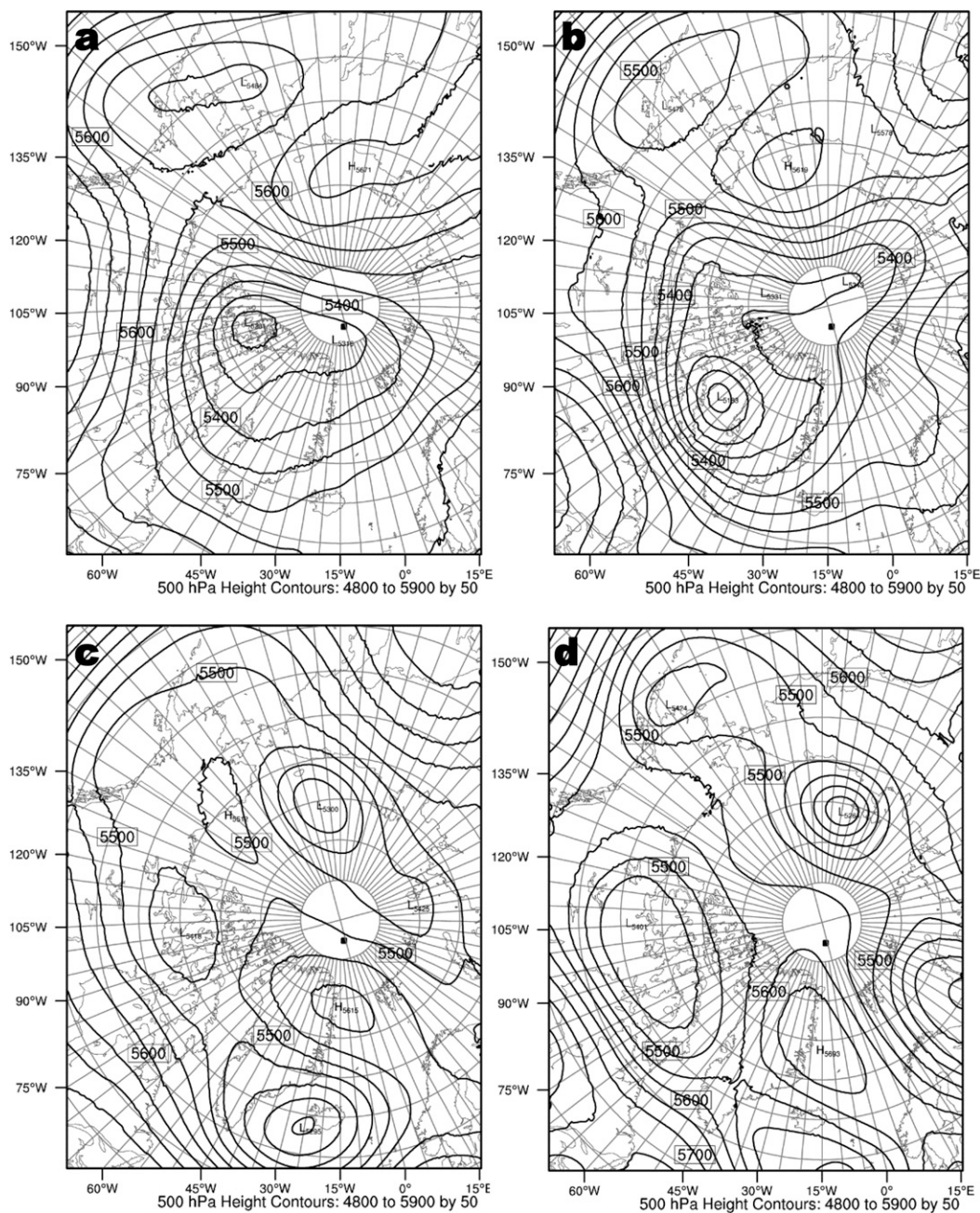


FIG. 4. Simulated 500-hPa geopotential height (geopotential meters, gpm) averaged over regimes (a) 1, (b) 2, (c) 3, and (d) 4. Contour interval is 50 gpm. The square is the mean location of the *Oden* during regimes 1–4.

4. Results of the control simulation

We now compare simulations with Polar WRF version 3.7.1 to the ASCOS observations. Model values are bilinearly interpolated from the nearest four grid points on the 3-km grid to the location of ASCOS. We begin with a Polar WRF simulation with standard settings, known as the Control simulation (Table 1). Figure 2

shows the vertical temperature profile below 600 hPa as a function of time for both radiosonde observations and hourly model output. The simulation reasonably captures both the vertical temperature profile above 900 hPa and the time variations from 10 August to 3 September. Consequently, data assimilation was not included during the 48-h segments. An inversion is frequently present with maximum temperature from 500 to

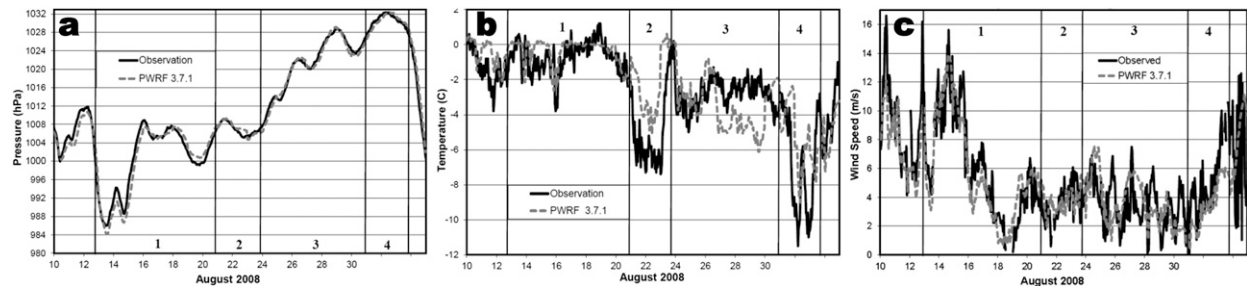


FIG. 5. Time series for (a) mean sea level pressure (hPa), (b) temperature ($^{\circ}\text{C}$), and (c) wind speed (m s^{-1}) at the *Oden* from observations (solid line) and the Control simulation (dashed line).

1500 m MSL. We will return to the vertical stratification later in this section. Several warmer periods are seen in the lower troposphere, including 11–13 August. Other warmer periods occurred on 16–19 August, 21–23 August, 26–29 August, and 2–3 September. The simulation is too cold in the lower troposphere on 20–21 August, and is insufficiently warm near 27 August. The temperature structure in the lower troposphere is strongly linked to low-level clouds (Sedlar et al. 2011; Tjernström et al. 2012). The overall agreement between Figs. 2a and 2b is encouraging for use of the ASCOS case to study the representation of Arctic low-level clouds in Polar WRF.

Figures 3 and 4 help to demonstrate the synoptic conditions during the four regimes at ASCOS. The average simulated fields of sea level pressure and 2-m temperature for each of the four regimes during ASCOS are shown in Fig. 3. Figure 4 shows the corresponding average 500-hPa height fields. During the first regime (13–20 August), a surface low is northwest of Greenland with a trough extending to the east to a region slightly south of the *Oden*'s position (Fig. 3a). A similar feature is seen at 500 hPa (Fig. 4a). The North Pole is in a region of moderately strong height gradient. Sedlar et al. (2012) discuss the importance of horizontal advection in the formation and maintenance of Arctic clouds, and Sedlar et al. (2011) found that trajectories to the *Oden* originated from the east and the Kara Sea during this regime. Weather at the *Oden* is impacted by the nearby low, and the observed and modeled surface pressures are relatively low during this time (Fig. 5a). Accordingly, several frontal systems contribute to deep tropospheric clouds observed at ASCOS during regime 1, especially near 13, 16, and 20 August (Sedlar et al. 2011; Tjernström et al. 2012). The simulated near-surface temperature is relatively uniform near the freezing point of freshwater over the Arctic pack ice (Fig. 3a). The time series of observed and simulated temperatures vary between 0° and -2°C during regime 1 (Fig. 5b).

Figure 6a shows the observed and modeled cloud fractions at ASCOS. WRF uses the parameterization of

Xu and Randall (1996) to represent the cloud fraction with key inputs from the condensate mixing ratio and relative humidity. The model cloud fraction in the Control simulation stays at 1 during regime 1 and the three regimes that follow. The modeled low cloud fraction (for levels below 2000 m MSL) is also 1, indicating persistent clouds in the lower troposphere. The observed cloud fraction stays near 1 during most hours of regime 1, but is often less than 1 during regimes 2 and 4. The Control has more average simulated liquid cloud water, 0.325 mm, during regime 1 than the other regimes (Fig. 6b). All regimes show considerably more liquid cloud water in the simulations than is measured by the microwave radiometer at most times. At times the microwave-radiometer value exceeds 0.5 mm, usually on occasions when precipitation was observed, which may have resulted in spurious values. The similarity of the modeled low cloud path to the modeled liquid cloud water path in Fig. 6b indicates that most of the cloud condensate is liquid and below 2000 m. The average cloud ice path during regime 1 is 0.0035 mm, two orders of magnitude less than the liquid cloud water path. Given that such a large fraction of the cloud condensate is liquid water in low clouds, we will concentrate our analysis on liquid cloud water, as that will have the largest impact on the surface radiative fluxes.

During regime 2 (0000 UTC 21 August–1200 UTC 23 August), the observed low-cloud cover was often tenuous, with some low clouds mostly below 500 m (Sedlar et al. 2011; Tjernström et al. 2012). Sedlar et al. (2011) noted that some cirrus were observed between 5000 and 9500 m, while the magnitudes of the longwave and shortwave cloud forcings at the surface were reduced from their values during regime 1 (Fig. 7). In the simulation, a cold region is located north and northwest of Greenland, and the 2-m temperature is impacted at ASCOS (Figs. 3b and 5b). The low pressure near Greenland is now more distant from the North Pole, and the surface pressure increases at ASCOS (Figs. 3b, 4b, and 5a). Observed trajectories to the surface at the

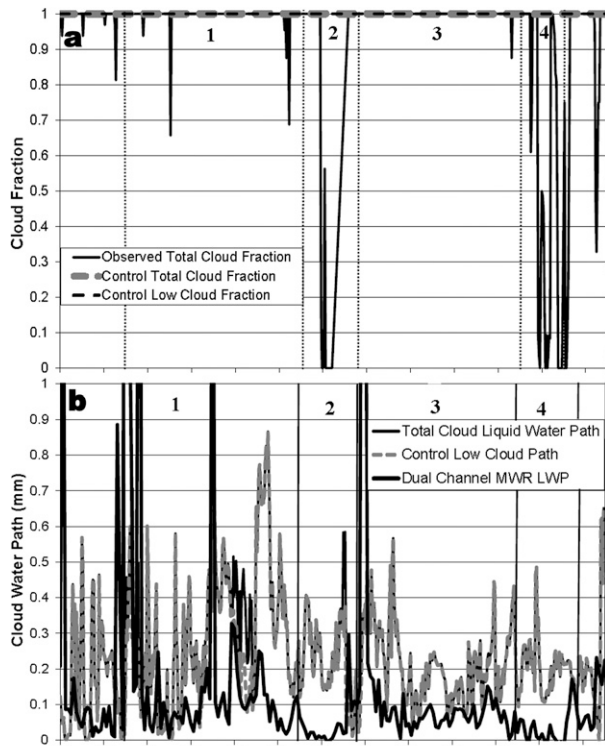


FIG. 6. Time series of (a) cloud fraction and (b) condensate path (mm). Total cloud fraction (solid line) in (a) is measured with a combination of vertically pointing remote sensors and obtained from Environment Climate Data Sweden, and total LWP (thick solid line) in (b) is from a dual-channel microwave radiometer. Also shown in (a) is the total cloud fraction and low cloud fraction from the Control simulation. The total cloud liquid water path and low cloud path from the Control simulation are shown in (b).

ASCOS site are from the vicinity of Greenland (Sedlar et al. 2011). The Control simulation does not capture the magnitude of the cooling seen in the observations (Fig. 5b). The observed temperature falls to about -7°C , while the simulated temperature only falls to about -4°C . The warm bias can be explained with the longwave cloud forcing at the surface. The average value of this quantity

during regime 2 is 47.8 W m^{-2} ; in the observations, however, the Control's value is 74.2 W m^{-2} . The magnitude of the shortwave cloud forcing is also excessive compared to the observations with a simulated value of -35.1 W m^{-2} compared to the observed -16.4 W m^{-2} . Figure 7 combined with Fig. 6b strongly indicates that excessively thick water clouds are leading to radiation errors that lead to the warm temperature bias during regime 2 (Fig. 5b).

During regime 3 (1200 UTC 23 August–30 August), the observed temperature initially increases to 0°C , then fluctuates between -2° and -4°C . (Fig. 5b). The observed clouds were not as thick as in the warmer regime 1, but low clouds, with tops approximately near 1 km, are deeper than in the colder regime 2. [See Sedlar et al.'s (2011) Fig. 3 and Tjernström et al.'s (2012) Fig. 21.] Observed trajectories are from the Fram Strait area to the south (Sedlar et al. 2011). For 27–29 August, the simulated 2-m temperature is about 2° – 3°C colder than the observed temperature at the *Oden*, suggesting that there are errors in the simulated surface energy balance that could be related to the cloud cover (Fig. 5b). The average total cloud forcing at the surface during this regime is 62.3 W m^{-2} in the observations; however, it is just 49.7 W m^{-2} in the Control run (Fig. 7c).

Regime 4 (31 August–1 September) is the coldest regime, with limited observed cloud cover, even in the boundary layer with some clouds below 300 m (Sedlar et al. 2011; Tjernström et al. 2012). Almost no cloud ice is simulated for this regime. Observed trajectories are taken from across the pole from the western Arctic (Sedlar et al. 2011). Similar to regime 2, the Control run does not fully capture the extent of the observed cooling during regime 4, as the simulated values for longwave cloud forcing and total cloud forcing are larger than the associated values from the observations (Fig. 7). While the observed temperature twice falls to about -11°C , the simulated temperature only once reaches about -9°C (Fig. 5b). Except for high-frequency variability, the simulation well captures the observed wind speed in all four

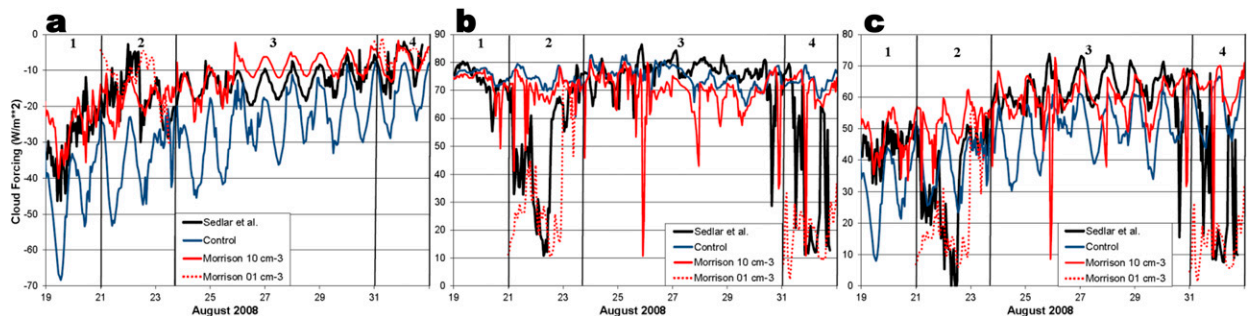


FIG. 7. Time series of surface cloud forcing (W m^{-2}) from Sedlar et al. (2011, solid black line), the Control (blue line), Morrison 10 cm^{-3} (red line), and Morrison 1 cm^{-3} (dashed red line) simulations: (a) shortwave cloud forcing, (b) longwave cloud forcing, and (c) total cloud forcing.

regimes at ASCOS, except for the wind speed maximum late on 2 September when the error can be as large as 4 m s^{-1} (Fig. 5c).

Figure 8 shows vertical profiles of temperature and equivalent potential temperature for the four regimes and the water and ice condensate for the full time period 10 August–3 September. The error in simulated temperature is much less than 1°C above 1500 m (Fig. 8a). The spectral nudging acts directly on the atmospheric temperature above 900 m and may reduce errors above the boundary layer. Because of time variations in the temperature inversion, the two coldest cases for 250–1250 m (regimes 3 and 4) are actually the warmest two cases above 1500 m. Forecast temperature errors tend to be greatest in and below the inversion layer. A shallow mixed layer below the inversion appears in the lowest 250 m during the regimes of the Control simulation and for some of the observed profiles in Fig. 8a. The largest errors are found during regime 2 with a cold bias of up to 2°C in the inversion. Clearly, the troposphere below 1500 m has the most variability and is more prone to simulation error.

Figure 8c offers insights into the average structure of the lower-tropospheric layer during the 10 August–3 September Control simulation. The vertical scale in Fig. 8c is greater than in Figs. 8a and 8b to demonstrate the vertical profile of ice clouds in the simulation. Because of much greater simulated mixing ratios for cloud liquid water than other condensate species in Fig. 8c, the mixing ratios for ice cloud and liquid rain are multiplied by 100, and the second most common condensate, snow ice, is multiplied by 10. A strong separation between simulated water clouds and simulated ice clouds is indicated in Fig. 8c. The great majority of the ice cloud condensate is located above 2000 m. The maximum cloud ice mixing ratio is approximately 0.0017 g kg^{-1} and is located above 7000 m MSL. Liquid condensate is strongly concentrated in low clouds and to a much lesser extent in middle clouds below 3000 m. The water cloud mixing ratio peaks about 0.25 g kg^{-1} near 200–300 m MSL, with a second, much weaker, maximum about 0.03 g kg^{-1} near 2100 m largely because of clouds during regime 1. Frozen condensate is present within the simulated low-level water clouds as a result of falling snow. The region below 1500 m with high temperature variability as demonstrated by Fig. 8a is dominated by liquid clouds (Fig. 8c). Consequently, the liquid water physics of the Morrison microphysics scheme is crucial for ASCOS simulations.

The vertical profiles of equivalent potential temperature θ_e shown in Fig. 8b are calculated from radiosonde observations and the Control run averaged for each of the four regimes. Here, θ_e is a useful diagnostic for the

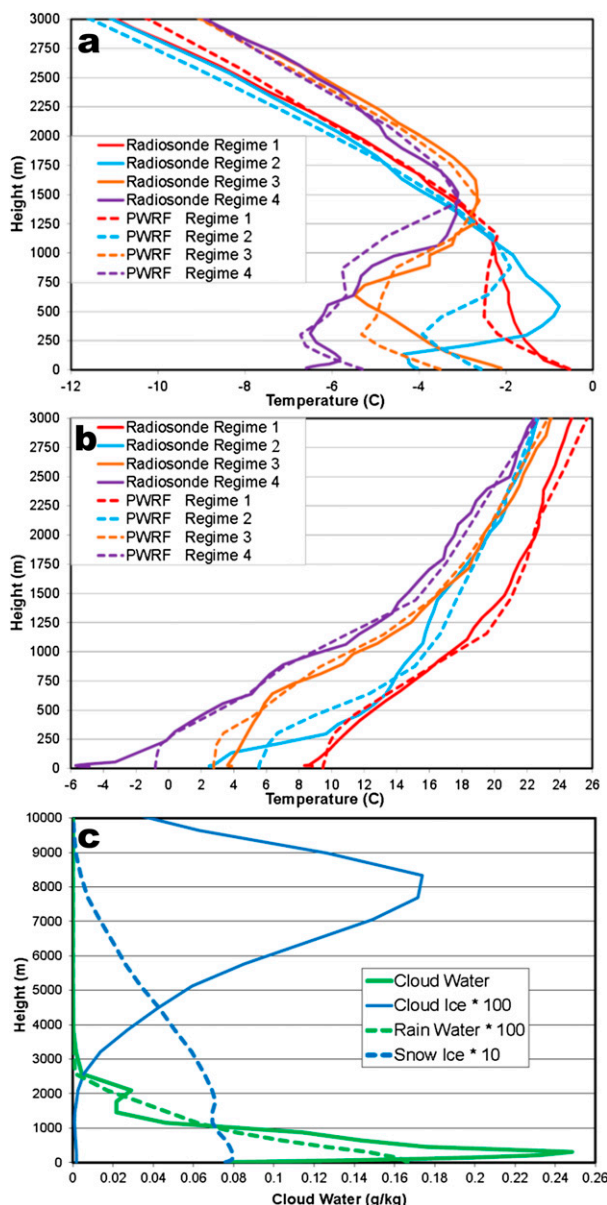


FIG. 8. Vertical profiles at ASCOS of (a) temperature ($^\circ\text{C}$) and (b) potential temperature ($^\circ\text{C}$) during the four regimes (see text) based upon radiosonde observations (solid lines) and the PWRf Control run (dashed lines), and (c) average PWRf condensate mixing ratio during 10 Aug–3 Sep. Snow ice (dashed blue line) is multiplied by 10, while cloud ice (solid blue line) and rainwater (dashed green line) are multiplied by 100.

vertical structure of Arctic low clouds that shows well-mixed layers where θ_e is approximately isothermal and stable layers where θ_e increases with height (Shupe et al. 2013). Low clouds during ASCOS were frequently detached from the surface because of interlayering stable layers (Sedlar et al. 2012; Shupe et al. 2013; Sedlar and Shupe 2014; Sotiropoulou et al. 2014). The observed

profile of θ_e is well represented by the Control simulation in the 250–1000-m layer during regime 4 (Fig. 8b). During regime 1, on the other hand, the near-surface profile in the Control run is insufficiently stable below 300 m. The simulated profile is too stable below 650 m for regime 3. Moreover, during regime 2 the observations show a very stable layer with a strong θ_e inversion below 300 m, while the Control profile shows a much weaker θ_e inversion. Furthermore, the Control run is too cold for 200–750 m, and this is reflected in Fig. 8a with the Control results having a cold bias of 2°C near 500 m. The results for regimes 1 and 2 show similarity to Birch et al.'s (2012) findings with the Met Office Unified Model (MetUM), which show the simulated near-surface was too well mixed in comparison to the ASCOS observations. We will return to the simulation of the vertical profile during regime 2 in the sensitivity experiments discussed in section 5.

Model performance statistics for the Control simulation are summarized in Table 2. Statistics for hourly near-surface state variables are calculated for 10 August–3 September, while statistics for hourly surface flux variables were calculated for 15–31 August when observed fluxes were available. The Control run results have small magnitude biases for surface pressure (−0.3 hPa) and temperature (0.4°C). The first terms in the columns for correlation and root-mean-square error (RMSE) are calculated based upon hourly values. The second terms are calculated from the daily averages. Figure 5 displays considerable high-frequency variability, so the correlations are greater and the RMSEs are smaller for the daily averages. The wind speed has a negative bias, but the correlations 0.80 (0.96) are quite large. Overall, the near-surface state variables are treated well by Polar WRF. For the surface turbulent fluxes, however, most of the mean errors can be explained by the contribution from positive biases. The magnitude of the observed turbulent fluxes was quite small at ASCOS, with average sensible heat flux (directed from the surface into the atmosphere) during 15–31 August estimated at 0.9 W m^{-2} while the latent heat flux was 1.9 W m^{-2} . In contrast, the average model values for the same time period are 6.5 and 4.9 W m^{-2} , respectively. The positive biases are consistent with the surface layer being too well mixed in the Control run. Moreover, the hourly correlations are 0.08 or smaller for the turbulent flux terms. Unlike that for the state variables, averaging these fluxes into daily values to reduce variability does not increase the correlation. The correlations for the daily average are both only 0.05.

Incorrect representation of the surface flux fields can contribute to, or possibly compensate for, errors in the surface radiation budget impacted by cloud cover. We

find that there is a large magnitude bias, -33.9 W m^{-2} , in the incident shortwave radiation at the surface (Table 2). Thus, the shortwave cloud forcing has excessive magnitudes in the Control simulation (Fig. 7a). It will be shown later that excessive liquid low-level cloud is contributing to this bias. This is in part mitigated by the smaller modeled than observed surface albedo over the sea ice during August (see Fig. 9) and the positive bias for incident longwave radiation (5.8 W m^{-2}). Since the temperature bias 0.4°C is modest for the Control run, it appears that other terms are compensating for the radiation errors. One error that draws our attention is the negative bias in surface albedo over the pack ice. Even though it is August, when we expect melt ponds to be widespread (e.g., Perovich et al. 2002), the observed albedo shown in Fig. 9 is surprisingly large. Values start near 0.7 on 15 August and quickly reach 0.83 within 2 days, before decreasing to 0.68 late on 19 August (Fig. 9).

Birch et al. (2012) argue that the observed value is actually representative of a $10 \text{ m} \times 10 \text{ m}$ area on the ice floe, while the average for an area the size of one of their model grid points (0.375° latitude \times 0.5625° longitude) would be decreased by accounting for approximately 20% of the surface water in melt ponds and leads, according to aerial photographs taken at the start of the ice camp. The observed albedo directly from the shortwave measurements quickly increases again after 19 August to above 0.8, and eventually becomes as large as 0.88 in regime 3. Widespread cloudiness during ASCOS could contribute to large observed albedo, as Key et al. (2001) find the surface albedo over snow/ice is about 0.05 greater under cloudy skies than under clear skies. In contrast, the albedo in the Control simulation stays below 0.70 until 29 August. Birch et al.'s corrected albedo is near 0.7 during regime 3, but this estimate may be low as the surface water froze up during the time of the ASCOS study. The sea ice fraction at ASCOS in our simulations, obtained from remote sensing observations, is greater than 99% during regime 3. While this value does not consider melt ponds, it suggests there are limited impacts of surface water on the albedo during the latter part of August.

Observers at the ASCOS site reported frequent new fallen snow on the ice, and that highly reflective surface cover can explain the sudden onset of large albedo at ASCOS (Tjernström et al. 2012). The Control albedo shown in Fig. 9 follows an imposed seasonal cycle for sea ice (Wilson et al. 2011). The imposed seasonal cycle, which is based upon the observed 1997–98 record at SHEBA, has typical August values near 0.65, characteristic of bare ice. The additional absorbed energy at the surface due to lower-than-observed albedo in the Control run may contribute to a slight warm bias near

TABLE 2. Model performance statistics in comparison to ASCOS observations. First values for correlation and RMSE are calculated from hourly values; the second values, in parentheses, are from daily averages. Statistics for near-surface state variables are for 0000 UTC 10 Aug–2300 UTC 3 Sep while those for surface flux terms are for 0000 UTC 15 Aug–2300 UTC 31 Aug.

Variable	Bias (model – observation)	Correlation	RMSE	Mean error
Control simulation				
Surface pressure (hPa)	–0.3	1.00 (1.00)	1.2 (1.1)	1.0
2-m temperature (°C)	0.4	0.69 (0.79)	1.9 (1.5)	1.4
10-m wind speed (m s ^{–1})	–0.30	0.80 (0.96)	2.0 (1.3)	1.6
2-m specific humidity (g kg ^{–1})	0.13	0.76 (0.86)	0.40 (0.30)	0.31
Sensible heat flux (W m ^{–2})	5.6	0.08 (0.05)	9.1 (7.9)	6.8
Latent heat flux (W m ^{–2})	3.1	0.05 (0.05)	6.1 (5.2)	4.4
Incident shortwave radiation (W m ^{–2})	–33.9	0.42 (0.36)	45.3 (37.7)	36.8
Incident longwave radiation (W m ^{–2})	5.8	0.41 (0.57)	19.1 (14.7)	11.0
Incident total radiation (W m ^{–2})	–28.1	0.55 (0.65)	39.1 (31.7)	32.2
Albedo (fraction)	–0.14	0.65 (0.70)	0.14 (0.14)	0.14
Snow Albedo simulation				
Surface pressure (hPa)	–0.2	1.00 (1.00)	1.2 (1.1)	1.0
2-m temperature (°C)	0.2	0.68 (0.77)	2.0 (1.5)	1.5
10-m wind speed (m s ^{–1})	–0.30	0.80 (0.96)	2.0 (1.2)	1.6
2-m specific humidity (g kg ^{–1})	0.09	0.75 (0.85)	0.41 (0.30)	0.32
Sensible heat flux (W m ^{–2})	5.3	0.09 (0.05)	8.6 (7.4)	6.5
Latent heat flux (W m ^{–2})	2.4	–0.02 (–0.03)	5.7 (4.8)	4.1
Incident shortwave radiation (W m ^{–2})	–27.8	0.42 (0.29)	41.1 (32.7)	31.5
Incident longwave radiation (W m ^{–2})	5.2	0.40 (0.54)	19.1 (14.7)	11.3
Incident total radiation (W m ^{–2})	–22.6	0.56 (0.61)	35.1 (27.1)	27.9
Albedo (fraction)	–0.05	0.73 (0.78)	0.06 (0.06)	0.05
Morrison 100 cm^{–3}				
Surface pressure (hPa)	–0.2	1.00 (1.00)	1.2 (1.1)	1.0
2-m temperature (°C)	0.2	0.67 (0.77)	2.0 (1.5)	1.5
10-m wind speed (m s ^{–1})	–0.30	0.79 (0.96)	2.0 (1.3)	1.6
2-m specific humidity (g kg ^{–1})	0.08	0.75 (0.85)	0.41 (0.30)	0.32
Sensible heat flux (W m ^{–2})	5.7	0.09 (0.06)	9.0 (7.8)	6.9
Latent heat flux (W m ^{–2})	2.8	–0.03 (–0.05)	6.0 (5.1)	4.4
Incident shortwave radiation (W m ^{–2})	–21.9	0.49 (0.36)	35.9 (27.2)	26.8
Incident longwave radiation (W m ^{–2})	4.7	0.38 (0.53)	19.3 (14.6)	11.5
Incident total radiation (W m ^{–2})	–17.2	0.63 (0.70)	30.3 (21.9)	23.8
Albedo (fraction)	–0.05	0.73 (0.78)	0.06 (0.06)	0.05
Morrison 50 cm^{–3}				
Surface pressure (hPa)	–0.2	1.00 (1.00)	1.2 (1.1)	1.0
2-m temperature (°C)	0.2	0.66 (0.76)	2.0 (1.6)	1.5
10-m wind speed (m s ^{–1})	–0.30	0.80 (0.96)	2.0 (1.3)	1.6
2-m specific humidity (g kg ^{–1})	0.07	0.75 (0.85)	0.41 (0.30)	0.32
Sensible heat flux (W m ^{–2})	6.0	0.08 (0.04)	9.4 (8.2)	7.2
Latent heat flux (W m ^{–2})	2.8	–0.03 (–0.07)	6.4 (5.4)	4.6
Incident shortwave radiation (W m ^{–2})	–15.9	0.56 (0.46)	31.2 (21.9)	22.5
Incident longwave radiation (W m ^{–2})	4.0	0.37 (0.50)	19.3 (14.8)	11.9
Incident total radiation (W m ^{–2})	–11.9	0.69 (0.77)	25.9 (16.9)	19.7
Albedo (fraction)	–0.05	0.73 (0.78)	0.06 (0.06)	0.05
Morrison 20 cm^{–3}				
Surface pressure (hPa)	–0.3	1.00 (1.00)	1.2 (1.1)	0.9
2-m temperature (°C)	0.1	0.64 (0.74)	2.1 (1.7)	1.6
10-m wind speed (m s ^{–1})	–0.30	0.80 (0.96)	2.0 (1.2)	1.6
2-m specific humidity (g kg ^{–1})	0.05	0.74 (0.84)	0.42 (0.31)	0.33
Sensible heat flux (W m ^{–2})	6.9	0.06 (0.02)	10.3 (9.2)	8.0
Latent heat flux (W m ^{–2})	3.0	–0.02 (–0.08)	6.6 (5.6)	4.8
Incident shortwave radiation (W m ^{–2})	–6.8	0.63 (0.60)	25.5 (14.6)	18.6
Incident longwave radiation (W m ^{–2})	2.7	0.35 (0.48)	19.6 (14.8)	12.5
Incident total radiation (W m ^{–2})	–4.1	0.76 (0.87)	21.0 (10.3)	16.0
Albedo (fraction)	–0.05	0.73 (0.78)	0.06 (0.06)	0.05

TABLE 2. (Continued)

Variable	Bias (model – observation)	Correlation	RMSE	Mean error
Morrison 10 cm ⁻³				
Surface pressure (hPa)	-0.3	1.00 (1.00)	1.2 (1.1)	0.9
2-m temperature (°C)	-0.1	0.64 (0.72)	2.2 (1.8)	1.6
10-m wind speed (m s ⁻¹)	-0.30	0.81 (0.96)	2.0 (1.2)	1.5
2-m specific humidity (g kg ⁻¹)	0.01	0.75 (0.83)	0.43 (0.33)	0.33
Sensible heat flux (W m ⁻²)	7.5	0.07 (0.00)	10.9 (9.9)	8.5
Latent heat flux (W m ⁻²)	3.3	-0.04 (-0.11)	6.9 (5.9)	5.0
Incident shortwave radiation (W m ⁻²)	-0.1	0.65 (0.68)	24.2 (11.9)	17.9
Incident longwave radiation (W m ⁻²)	0.2	0.39 (0.51)	19.4 (14.4)	13.3
Incident total radiation (W m ⁻²)	0.1	0.79 (0.90)	19.9 (9.7)	15.3
Albedo (fraction)	-0.05	0.73 (0.78)	0.06 (0.06)	0.05

the surface and the excessive turbulent fluxes into the atmosphere (Table 2).

Since we seek improved surface fluxes as a contribution toward improved linkages between the surface and lower-tropospheric clouds, and since errors in the fluxes may bias the clouds which are our primary interest, we conduct a new simulation with a modified surface albedo. The new simulation termed Snow Albedo (Table 1) has the same specifications as the Control simulation except that the albedo for the ice fraction of sea ice grid points is determined from a new formula inspired by the ASCOS observations:

$$\text{Albedo}_{\text{sea ice}} = 0.82 \text{ for } \text{Snow} > 0.01, \quad (1)$$

$$\text{Albedo}_{\text{sea ice}} = 0.70 \text{ for } \text{Snow} < 0.001, \quad (2)$$

otherwise

$$\text{Albedo}_{\text{sea ice}} = [0.82(\text{Snow} - 0.001) + 0.70(0.01 - \text{Snow})]/(0.01 - 0.001), \quad (3)$$

where $\text{Albedo}_{\text{sea ice}}$ is the albedo for the ice fraction and Snow is the instantaneous snow depth on the ice in meters. The minimum $\text{Albedo}_{\text{sea ice}}$ is now increased to 0.7, and only a small amount of snow is required to change the sea ice albedo to its maximum value of 0.82. The total gridpoint albedo may be less than 0.7 because of the open-water fraction. Figure 9 shows that the modified albedo formula still produces a value less than the observed value at ASCOS during most of the latter half of August, but that observed value may be unrealistically high for mesoscale applications according to Birch et al. (2012). Nevertheless, the modified albedo is much closer to the observations than the Control value. Note that this formula is applied for all grid points that have sea ice, not just those near ASCOS. Therefore, we preferred a conservative modification to the sea ice albedo.

Time series for the new simulation Snow Albedo are shown in Fig. 10. Table 2 shows that while the magnitudes of the biases for surface pressure, 2-m temperature,

and 2-m specific humidity are at least slightly decreased, the correlations and RMSEs for the state variables are in general not improved by the change. Figure 10 shows simulated 2-m specific humidity in comparison to observations at ASCOS. Near 29 August, the smallest error is actually found in the Control run. The dry bias at this time has larger magnitudes in other simulations. At other times, the near-surface specific humidity shows little difference between simulations. The deficit for incident shortwave is decreased by 6.1 W m⁻² with the new simulation suggesting that modifications can help produce a better cloud simulation.

5. Sensitivity tests

Parameter adjustments to the Morrison two-moment microphysics scheme are sought to better simulate the Arctic clouds observed at ASCOS. Here, we draw upon earlier work by Luo et al. (2008) and Morrison et al. (2008) that demonstrates considerable sensitivity to certain specifications within the cloud physics scheme. While Luo et al. (2008) found that increasing the ice

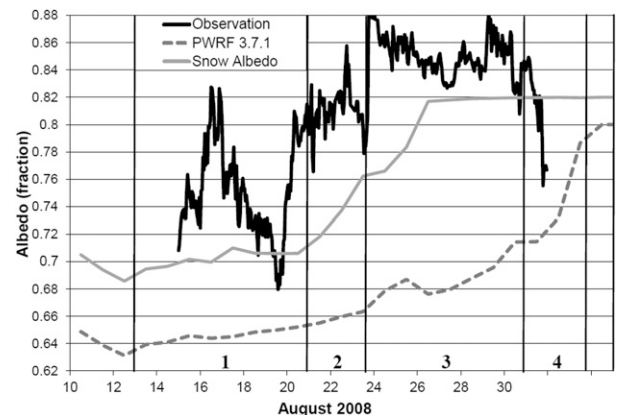


FIG. 9. Time series of surface albedo (fraction) adjacent to the Oden for observations (solid black line), the Control simulation (dashed gray line), and the Snow Albedo simulation (solid gray line).

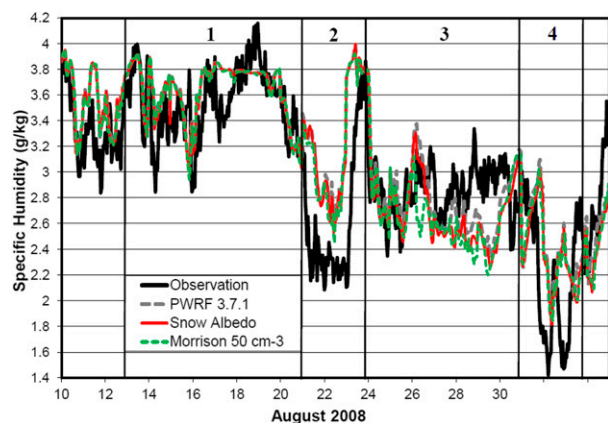


FIG. 10. Time series of 2-m specific humidity (g kg^{-1}) at the *Oden* for observations (solid black line), and the Control (dashed gray line), Snow Albedo (red line), and Morrison 50 cm^{-3} (dashed green line) simulations.

nuclei concentration weakened mixed-phase clouds, Morrison et al. (2008) found that LWP increased as CCN concentrations increased. Furthermore, Birch et al. (2012) ran tests with a single-column version of the MetUM and simulated improved vertical profiles of temperature and cloud for regime 4 during ASCOS when they reduced the CCN concentration toward values representative of the tenuous cloud regime (e.g., 1 cm^{-3}). The Regional Arctic System Model (RASm; Roberts et al. 2015) modified the Morrison scheme's specified liquid cloud droplet concentration from the standard value of 250 cm^{-3} more characteristic of lower-latitude conditions to 50 cm^{-3} for their Arctic simulations (J. Cassano 2015, personal communication).

Fortunately, observations of cloud-forming aerosols were a key goal for the ASCOS project. ASCOS observations show that CCN concentrations can occasionally be smaller than 1 cm^{-3} , though the concentration was larger than 10 cm^{-3} about 75% of the time (Martin et al. 2011; Mauritsen et al. 2011; Tjernström et al. 2014; Leck and Svensson 2015). The value 100 cm^{-3} is an approximate maximum concentration during ASCOS. Consequently, we run four sensitivity tests with specified liquid droplet concentrations set at 10, 20, 50, and 100 cm^{-3} and compare results to Control and Snow Albedo that have a setting of 250 cm^{-3} (Table 1). An additional test with the specified liquid droplet concentration set at 1 cm^{-3} is run for regimes 2 and 4 when tenuous clouds were observed (Sedlar et al. 2011; Mauritsen et al. 2011). The value 1 cm^{-3} is a reasonable setting for regime 4 (Mauritsen et al. 2011), and Kupiszewski et al. (2013) suggest that aerosol concentrations in the lowest few hundred meters during regime 2 were about double those of regime 4.

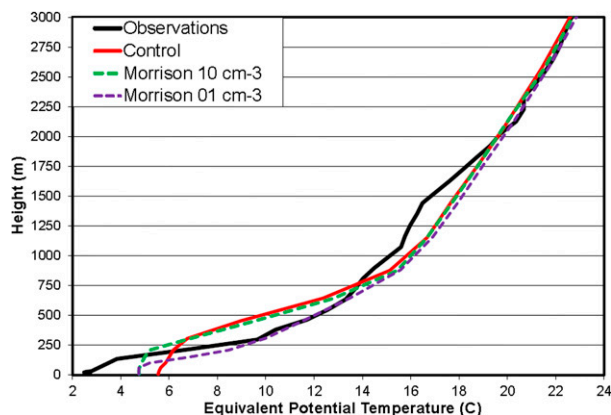


FIG. 11. Vertical profiles at ASCOS of average equivalent potential temperature ($^{\circ}\text{C}$) during regime 2 for radiosonde observations and PWRf simulations.

For simplicity, we use 1 cm^{-3} in both cases. The five new simulations use the same sea ice albedo as in Snow Albedo for a better representation of the radiative fluxes at ASCOS.

First, we return to the equivalent potential temperature profile in the lower troposphere previously shown in Fig. 8b. Selected sensitivity test results for regime 2 are shown in Fig. 11. As we saw previously, the strong θ_e near-surface inversion in the radiosonde profile is not simulated in the Control run. The Morrison 10 cm^{-3} simulation has a liquid droplet concentration much closer to the observed CCN for the tenuous cloud regime, but produces a θ_e vertical profile that is only a slight improvement over that of the Control simulation. The near-surface temperature is about 1°C colder than the Control result, but the profile is still much too well mixed below 300 m. The Morrison 1 cm^{-3} simulation, however, which has a realistic liquid droplet concentration for the tenuous cloud regime, shows much better agreement with the observed profile below 640 m, even though there is still a warm bias near the surface. The warm bias above 750 m is slightly increased in the Morrison 1 cm^{-3} simulation, but there is a strong θ_e inversion above 100 m, demonstrating strong static stability, albeit not as large as that of the radiosonde profile. This demonstrates how changing the Arctic low-level clouds can alter the boundary layer. Correspondingly, improvement in longwave cloud forcing for the tenuous cloud regimes during regimes 2 and 4 is seen in Fig. 7b. The Morrison 1 cm^{-3} simulation shows a longwave cloud forcing that is often about 40 W m^{-2} less than that of the Control run.

For the range of conditions observed during the ASCOS study, Table 2 shows that reducing the liquid droplet concentration produces a much improved simulation of the radiative flux at ASCOS. The incident shortwave bias is changed from -27.8 W m^{-2} in Snow

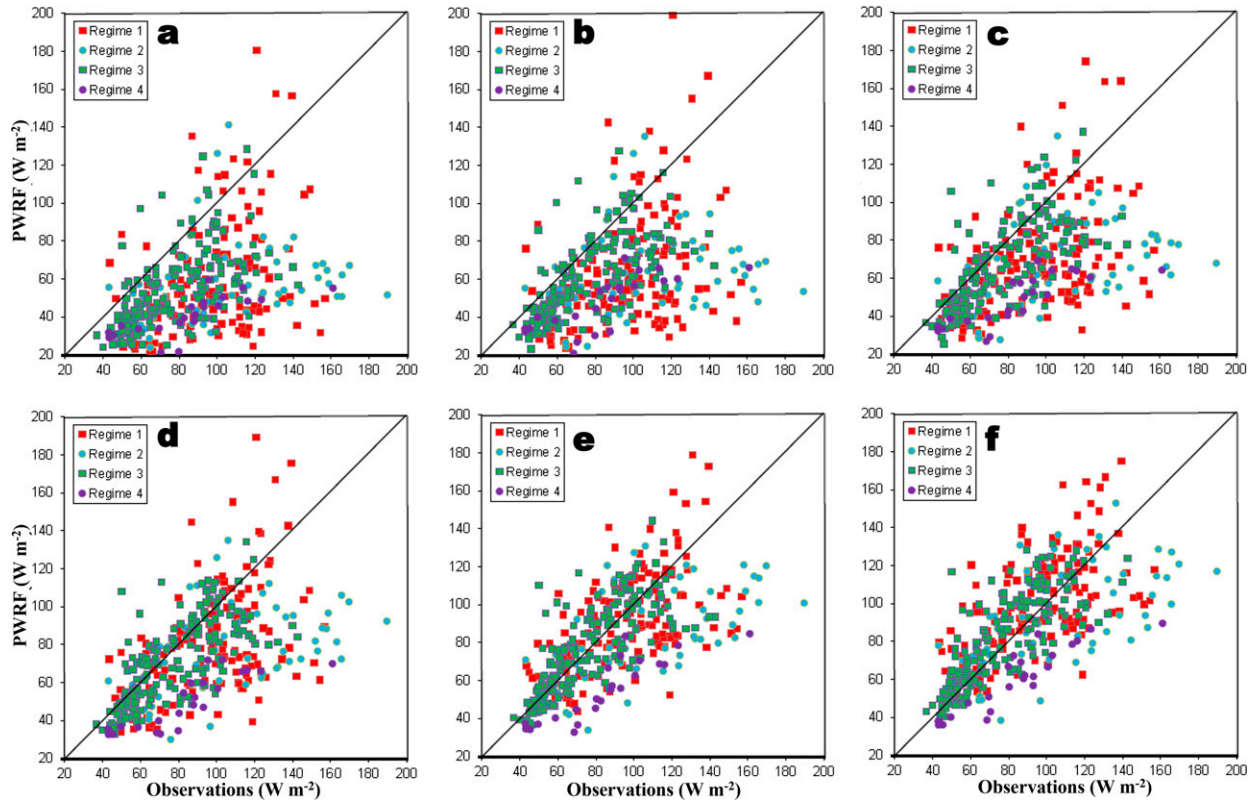


FIG. 12. Scatterplots of simulated vs observed hourly incident shortwave radiation (W m^{-2}) for the (a) Control, (b) Snow Albedo, (c) Morrison 100 cm^{-3} , (d) Morrison 50 cm^{-3} , (e) Morrison 20 cm^{-3} , and (f) Morrison 10 cm^{-3} simulations at ASCOS during 15–31 Aug 2008.

Albedo to -21.9 , -15.9 , -6.8 , and -0.1 W m^{-2} in the simulations referred to as Morrison 100 cm^{-3} , Morrison 50 cm^{-3} , Morrison 20 cm^{-3} , and Morrison 10 cm^{-3} , respectively. Correspondingly, the magnitude of the shortwave cloud forcing in the Morrison 10 cm^{-3} run is approximately half that of the Control simulation (Fig. 7a). Moreover, the incident longwave bias, while not as large in magnitude, is reduced. The bias in longwave radiation for the Morrison 20 cm^{-3} and Morrison 10 cm^{-3} runs are 2.7 and 0.2 W m^{-2} , respectively, which are well within the estimated observational error of about 4 W m^{-2} (Sedlar et al. 2011). Longwave radiation is less sensitive than shortwave radiation to changes in droplet concentration, consistent with Thompson and Eidhammer (2014). The correlation for the hourly shortwave radiation also increases, from 0.42 in Snow Albedo to 0.49 , 0.56 , 0.63 , and 0.65 in the Morrison 100 cm^{-3} , Morrison 50 cm^{-3} , Morrison 20 cm^{-3} , and Morrison 10 cm^{-3} simulations, respectively. The correlation for hourly longwave radiation, however, is not consistently increased in the sensitivity simulations. The root-mean-square errors in the Morrison 10 cm^{-3} run for incident shortwave radiation are about half those of the simulations using liquid droplet concentrations of 250 cm^{-3} .

The changes, however, do not produce an overall improvement in the simulation of the state variables. The Control and Snow Albedo simulations have similar or slightly smaller root-mean-square errors for pressure, temperature, wind speed, and specific humidity (Table 2). Changing the surface albedo and reducing the CCN can remove most of the bias in 2-m temperature and 2-m specific humidity. Figure 10 shows that during 27–29 August within regime 3, the negative error for specific humidity is slightly increased in the sensitivity test. During those three days the bias is -0.30 g kg^{-1} in the Control run and -0.41 g kg^{-1} in the Morrison 50 cm^{-3} simulation. Simply reducing the radiation error does not necessarily alleviate other errors in the forecast. A different result in the simulations of the ASCOS study period was found by Sotiropoulou et al. (2016) when they included a new prognostic cloud scheme in the European Centre for Medium-Range Weather Forecasts Integrated Forecast System. The new scheme tended to increase liquid cloud water and reduce cloud ice, which alleviated previous biases. Analogous to our Control run, their simulated clouds tended to be too optically thick. Dissimilar to our case, the changes did not produce notable improvements in their simulation

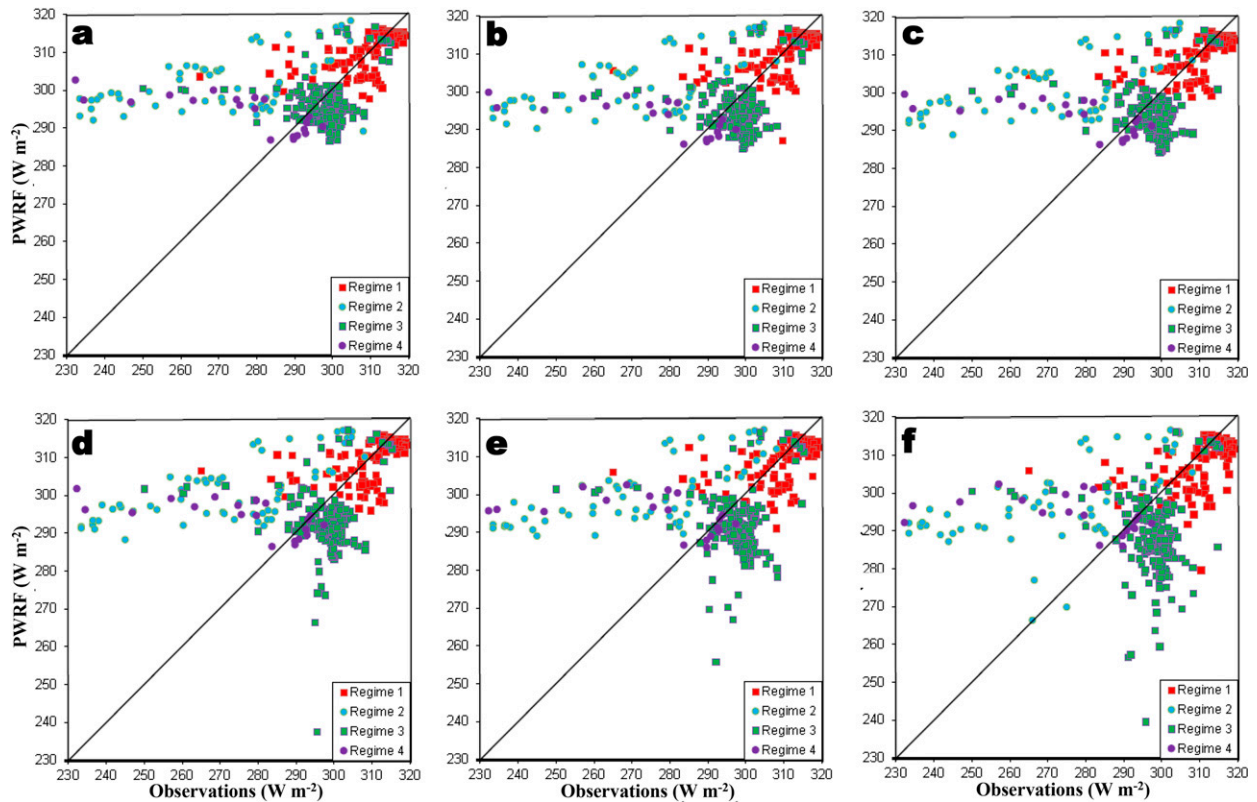


FIG. 13. Scatterplots of simulated vs observed hourly incident longwave radiation (W m^{-2}) for the (a) Control, (b) Snow Albedo, (c) Morrison 100 cm^{-3} , (d) Morrison 50 cm^{-3} , (e) Morrison 20 cm^{-3} , and (f) Morrison 10 cm^{-3} simulations at ASCOS during 15–31 Aug 2008.

of longwave and shortwave radiation, as the biases increased for both the incident longwave and shortwave radiation.

Figure 12 shows scatter diagrams for the incident shortwave radiation. The biases for incident solar radiation for the Control and Snow Albedo simulations are -33.9 and -27.8 W m^{-2} , respectively, as about 90% of the points in Figs. 12a and 12b fall to the right of the one-to-one line. A clear bias appears to be present over the range of observed values, especially for regime 4. The reduction in cloud droplet concentration improves the values for modeled shortwave radiation in Figs. 12c–f. The best clustering of modeled values near the observed ones is seen for the Morrison 20 cm^{-3} and Morrison 10 cm^{-3} simulations in Figs. 12e and 12f, corresponding to the smallest RMSE in Table 2. Nevertheless, negative biases are still apparent for regimes 2 and 4. There is a tendency in the sensitivity experiments for observed incident shortwave values over 125 W m^{-2} to correspond to modeled values at least 20 W m^{-2} less. This is probably due to the model producing more cloud cover when the observed cloud cover was limited, especially during regimes 2 and 4 (see Fig. 6).

Figure 13 shows the incident longwave radiation at the surface. Because of the extensive cloud cover at ASCOS, the observed longwave radiation usually exceeds 280 W m^{-2} . Longwave biases are smaller than those of shortwave radiation, and there is less difference between the simulations. This implies that while the shortwave results shown in Fig. 12 and Table 2 suggest optically thinner clouds in the sensitivity experiments, the clouds still act as essentially blackbody emitters of longwave radiation. There is a strong clustering in all cases near $295\text{--}300 \text{ W m}^{-2}$ observed and $280\text{--}300 \text{ W m}^{-2}$ simulated, apparently as result of the presence of boundary layer clouds, with simulated values tending to be smaller in the sensitivity tests. When observed values are below 280 W m^{-2} , the simulations tend to highly overpredict incident longwave radiation at the surface, especially during regimes 2 and 4 (Fig. 13). Analogous to the shortwave results, this suggests the model has difficulty with optically thinner cases.

Figure 14 shows the liquid water path estimated from the microwave radiometer observations and the simulated cloud liquid water for the simulations. The large majority of the cloud liquid water simulated by Polar

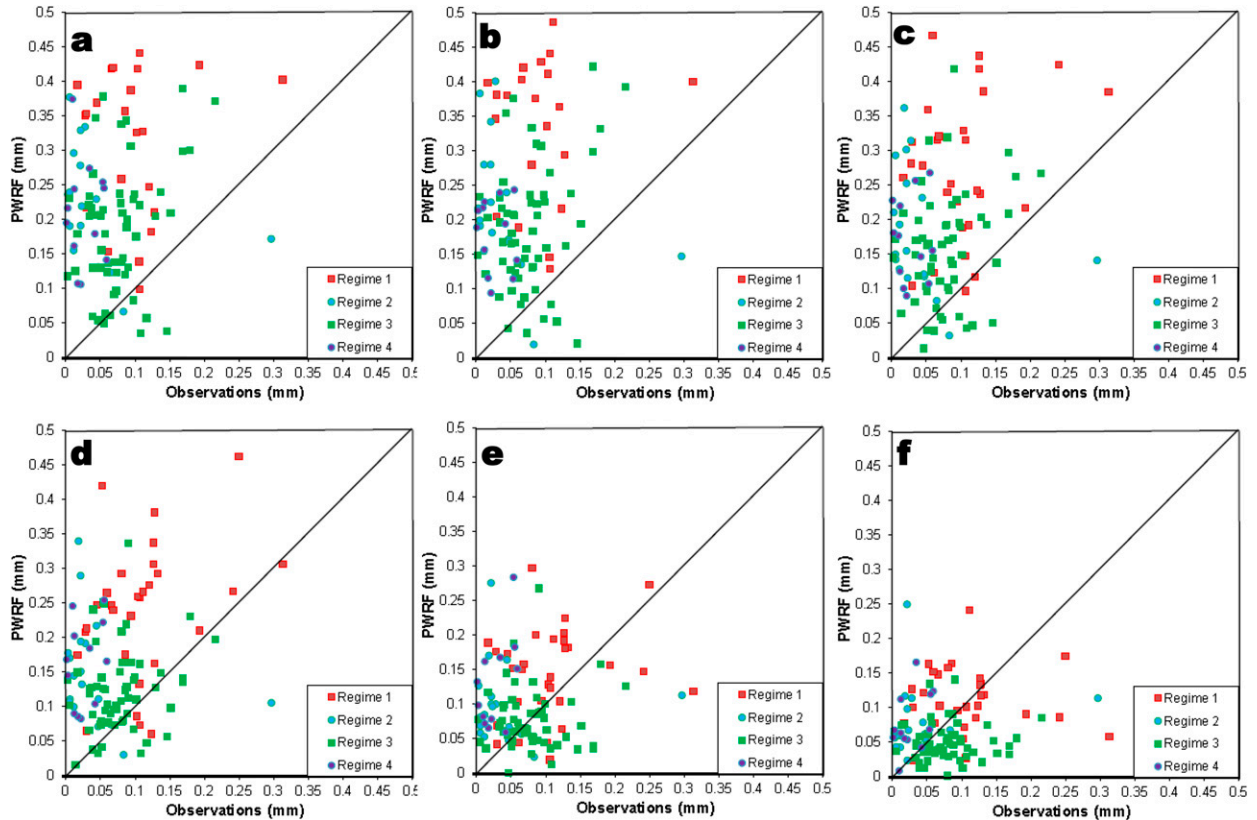


FIG. 14. Scatterplots of simulated vs observed LWC (mm) for the (a) Control, (b) Snow Albedo, (c) Morrison 100 cm^{-3} , (d) Morrison 50 cm^{-3} , (e) Morrison 20 cm^{-3} , and (f) Morrison 10 cm^{-3} simulations at ASCOS during 10 Aug–3 Sep 2008.

WRF is contained within low clouds (Fig. 8c). Thinner middle clouds, composed primarily of ice, are occasionally present. For Figs. 14a–d, the simulations regularly show more liquid water than the observations. Only for the Morrison 20 cm^{-3} and Morrison 10 cm^{-3} simulations are the values clustering around the one-to-one line (Figs. 14e,f). These simulations have fewer times with cloud liquid water content greater than 0.3 mm than any other simulation. We remove from the observations extreme positive values (greater than 0.3 mm) that correspond to observed precipitation according to the Vaisala FD12P weather sensor. The average liquid water content for the observations between 10 August and 3 September is 0.114 mm . The averages at the same times for the Control, Snow Albedo, Morrison 100 cm^{-3} , Morrison 50 cm^{-3} , Morrison 20 cm^{-3} , and Morrison 10 cm^{-3} simulations are 0.237 , 0.241 , 0.191 , 0.153 , 0.101 , and 0.073 mm . The Morrison 20 cm^{-3} run, which is representative of relatively pristine conditions, has an average cloud liquid water content within the uncertainty, about 0.025 mm , of the average from the microwave radiometer. Clearly, adjustments to the two-moment Morrison microphysics scheme are able to greatly alleviate

biases in cloud optical depth. The sensitivity test with droplet concentration reduced from 250 to 20 cm^{-3} produces realistic cloud water amounts and realistic radiative transfer through clouds.

Table 3 provides insight into how the modifications impact the simulations. Model values of liquid precipitation (probably supercooled drizzle from shallow stratiform clouds) reaching the surface interpolated horizontally to the drifting *Oden* increase in all four regimes as the specified liquid droplet concentration is reduced below 100 cm^{-3} to 10 cm^{-3} . The liquid cloud source of this precipitation is primarily below 1500 m (Fig. 8c). The rain water mixing ratio in the low cloud layer increases in the sensitivity tests with smaller concentrations of droplets (not shown). The increase in liquid precipitation is most striking during regime 4 when rates of 0.11 and 0.47 mm day^{-1} are simulated for the Morrison 100 cm^{-3} and Morrison 10 cm^{-3} runs, respectively. A further reduction of droplet concentration to 1 cm^{-3} dissipates the liquid water cloud (not shown) and reduces the liquid precipitation rate to 0.14 mm day^{-1} . Otherwise, the increased rain removes moisture from the lower troposphere. Measurements of observed precipitation

TABLE 3. Simulated large-scale liquid precipitation (mm day^{-1}) during ASCOS regimes.

Regime and period	Control	Morrison 100 cm^{-3}	Morrison 50 cm^{-3}	Morrison 20 cm^{-3}	Morrison 10 cm^{-3}
1: 13–20 Aug	0.62	0.50	0.64	0.75	0.86
2: 21–23 Aug	0.34	0.33	0.38	0.50	0.58
3: 23–30 Aug	0.12	0.17	0.23	0.32	0.36
4: 31 Aug–1 Sep	0.08	0.11	0.17	0.41	0.47
10 Aug–3 Sep	0.36	0.35	0.44	0.55	0.63

during regime 4 by the capacitive sensor on the Vaisala FD12P show precipitation, primarily in snow grains, at times on 31 August and 1 September. Observed precipitation rates are usually less than 0.1 mm h^{-1} , and the total accumulated precipitation from the sensor was suggested to be less than 0.1 mm. The cloud and precipitation processes at ASCOS during regime 4 are influenced by the very low aerosol content during this time period (Mauritsen et al. 2011).

The scatter in Fig. 14f remains large even with the reduced droplet concentration. Some scatter may arise from the uncertainty of the liquid water path retrievals by the microwave radiometer. Nevertheless, the model frequently fails to capture the instantaneous cloud water, and this is shown in the radiative fields impacted by the clouds. Accordingly, the RMSEs of state variables are not consistently improved by the changes to the model microphysics (Table 2). The changes, however, improve the climatic realism of the Polar WRF simulations.

6. Conclusions

Numerical simulations of the August–September 2008 ASCOS intensive observational study in the high Arctic near the North Pole have explored the realism of Polar WRF V3.7.1 depictions of low-level Arctic clouds, and more importantly, the impact these simulated clouds have on the surface energy budget. Polar WRF is run for 10 August–3 September 2008 on a nested grid system with an outer domain at 27-km spacing and nested domains at 9- and 3-km spacings. First, a Control simulation is run with standard Polar WRF settings including a specified seasonal sea ice albedo cycle. Additional simulations are run with sea ice albedo adjusted, based upon snow depth, to more closely represent the surprisingly high late-summer albedo measured during ASCOS.

The model very reasonably simulates the state variables surface pressure, near-surface temperature, near-surface specific humidity, and near-surface wind speed. The largest forecast temperature error and variability within the simulations are located in the lowest 1500 m. Correspondingly, simulating the extensive low-level clouds in the Arctic has proven to be a challenge for mesoscale and global models, and Polar WRF with the

standard version of the two-moment Morrison microphysics scheme simulates excessive optically thick Arctic clouds in comparison to ASCOS observations. This results in a deficit in incident shortwave radiation at the surface by about 30 W m^{-2} . Incident longwave radiation is less impacted; however, there is also a slight positive bias for this quantity.

Previous work suggests that the microphysics scheme is sensitive to the specified liquid droplet concentration. The standard value, 250 cm^{-3} , is geared toward low-latitude applications and may not be appropriate for many polar applications. Observations at ASCOS indicate CCN concentrations are between about 10 and 100 cm^{-3} 75% of the time, with occasional values near or below 1 cm^{-3} (Martin et al. 2011; Mauritsen et al. 2011; Tjernström et al. 2014; Leck and Svensson 2015). Based upon the observed CCN concentrations, we run sensitivity tests with specified liquid droplet concentrations of 1, 10, 20, 50, and 100 cm^{-3} . We find that reducing the droplet concentration increases the liquid precipitation and reduces the liquid water path of simulated Arctic clouds. Accordingly, incident shortwave radiation is increased and incident longwave radiation is slightly reduced. The Morrison 10 cm^{-3} and Morrison 20 cm^{-3} simulations, which represent very pristine Arctic conditions, have the largest impacts and the smallest radiation biases over the entire ASCOS period. The Morrison 1 cm^{-3} simulation for ASCOS regimes 2 and 4 more closely represents the tenuous cloud regime, when cloud formation is limited by a lack of available CCN (Mauritsen et al. 2011). Improving the simulated radiative fluxes by reducing the liquid droplet concentration, however, results in little improvement to the simulated state variables in comparison to the ASCOS observations. Errors in the near-surface fields may remain as a result of errors in the sensible and latent heat fluxes (Table 2). For skillful Arctic low-cloud predictions models will need accurate CCN predictions, along with microphysics schemes that incorporate prognostic CCN.

Acknowledgments. This research is supported by NASA Grants NNX12AI29G and NNH14CK47C. Numerical simulations were performed on the Intel Xeon cluster at the Ohio Supercomputer Center, which is

supported by the State of Ohio, and on NCAR's Computational and Information Systems Laboratory's Yellowstone, supported by NSF. The authors are grateful to the ASCOS Chief Scientists Michael Tjernstrom and Caroline Leck and their science team, to the captain of the *Oden*, Mattias Peterson, and his crew, and to the Swedish Polar Research Secretariat, for making the ASCOS data possible. We thank Gijs de Boer and Ola Persson for supplying and meticulously quality-controlling ASCOS surface flux data and Joseph Sedlar for supplying cloud forcing. Radiosonde and microwave radiometer data and weather observations from the *Oden* for ASCOS are available online (<http://www.ascos.se>). Precipitation estimates from the Vaisala FD12P weather sensor were supplied by Jussi Paatero of the Finnish Meteorological Institute. Cloud fraction was obtained from Environment Climate Data Sweden. We also thank Jinlun Zhang and Ron Lindsay of the University of Washington for supplying PIOMAS thickness and snow depth for sea ice and Jonas Mortin of Stockholm University for supplying sea ice freeze and thaw dates. Eli Mlawer provided valuable discussion on RRTMG's capabilities.

REFERENCES

- Barlage, M., and Coauthors, 2010: Noah land model modifications to improve snowpack prediction in the Colorado Rocky Mountains. *J. Geophys. Res.*, **115**, D22101, doi:10.1029/2009JD013470.
- Barton, N. P., S. A. Klein, J. S. Boyle, and Y. Y. Zhang, 2012: Arctic synoptic regimes: Comparing domain-wide Arctic cloud observations with CAM4 and CAM5 during similar dynamics. *J. Geophys. Res.*, **117**, D15205, doi:10.1029/2012JD017589.
- Birch, C. E., and Coauthors, 2012: Modelling atmospheric structure, cloud and their response to CCN in the central Arctic: ASCOS case studies. *Atmos. Chem. Phys.*, **12**, 3419–3435, doi:10.5194/acp-12-3419-2012.
- Bromwich, D. H., K. M. Hines, and L.-S. Bai, 2009: Development and testing of Polar WRF: 2. Arctic Ocean. *J. Geophys. Res.*, **114**, D08122, doi:10.1029/2008JD010300.
- , F. O. Otieno, K. Hines, K. Manning, and E. Shilo, 2013: Comprehensive evaluation of Polar Weather Research and Forecasting Model performance in the Antarctic. *J. Geophys. Res.*, **118**, 274–292, doi:10.1029/2012JD018139.
- Cassano, J. J., M. E. Higgins, and M. W. Seefeldt, 2011: Performance of the Weather Research and Forecasting (WRF) Model for month-long pan-Arctic simulations. *Mon. Wea. Rev.*, **139**, 3469–3488, doi:10.1175/MWR-D-10-05065.1.
- Cesana, G., J. E. Kay, H. Chepfer, J. M. English, and G. de Boer, 2012: Ubiquitous low-level liquid-containing Arctic clouds: New observations and climate model constraints from CALIPSO-GOCCP. *Geophys. Res. Lett.*, **39**, L20804, doi:10.1029/2012GL053385.
- Chapman, W. L., and J. E. Walsh, 2007: Simulations of Arctic temperature and pressure by global coupled models. *J. Climate*, **20**, 609–632, doi:10.1175/JCLI4026.1.
- Clough, S. A., M. W. Shephard, E. J. Mlawer, J. S. Delamere, M. J. Iacono, K. Cady-Pereira, S. Boukabara, and P. D. Brown, 2005: Atmospheric radiative transfer modeling: A summary of the AER codes. *J. Quant. Spectrosc. Radiat. Transfer*, **91**, 233–244, doi:10.1016/j.jqsrt.2004.05.058.
- Curry, J. A., W. B. Rossow, D. Randall, and J. L. Schramm, 1996: Overview of Arctic cloud and radiation characteristics. *J. Climate*, **9**, 1731–1764, doi:10.1175/1520-0442(1996)009<1731:OOACAR>2.0.CO;2.
- de Boer, G., W. Chapman, J. E. Kay, B. Medeiros, M. D. Shupe, S. Vavrus, and J. Walsh, 2012: A characterization of the present-day Arctic atmosphere in CCSM4. *J. Climate*, **25**, 2676–2695, doi:10.1175/JCLI-D-11-00228.1.
- , and Coauthors, 2014: Near-surface meteorology during the Arctic Cloud Ocean Study (ASCOS): Evaluation of re-analyses and global climate models. *Atmos. Chem. Phys.*, **14**, 427–445, doi:10.5194/acp-14-427-2014.
- Dee, D. P., and Coauthors, 2011: The ERA-Interim reanalysis: Configuration and performance of the data assimilation system. *Quart. J. Roy. Meteor. Soc.*, **137**, 553–597, doi:10.1002/qj.828.
- Eastman, R., and S. G. Warren, 2010: Interannual variations of Arctic cloud types in relation to sea ice. *J. Climate*, **23**, 4216–4232, doi:10.1175/2010JCLI3492.1.
- Ebert, E., and J. A. Curry, 1993: An intermediate one-dimensional thermodynamic sea ice model for investigating ice-atmosphere interactions. *J. Geophys. Res.*, **98**, 10 085–10 109, doi:10.1029/93JC00656.
- English, J. M., J. E. Kay, A. Gettelman, X. Liu, Y. Wang, Y. Zhang, and H. Chepfer, 2014: Contributions of clouds, surface albedos, and mixed-phase ice nucleation schemes to Arctic radiation biases in CAM5. *J. Climate*, **27**, 5174–5197, doi:10.1175/JCLI-D-13-00608.1.
- Forbes, R. M., and M. Ahlgrimm, 2014: On the representation of high-latitude boundary layer mixed-phase cloud in the ECMWF global model. *Mon. Wea. Rev.*, **142**, 3425–3445, doi:10.1175/MWR-D-13-00325.1.
- Francis, J. A., and E. Hunter, 2006: New insight into the disappearing Arctic sea ice. *Eos, Trans. Amer. Geophys. Union*, **87**, 509–511, doi:10.1029/2006EO460001.
- , D. M. White, J. J. Cassano, W. J. Gutowski Jr., L. D. Hinzman, M. M. Holland, M. A. Steele, and C. J. Vörösmarty, 2009: An Arctic hydrologic system in transition: Feedbacks and impacts on terrestrial, marine, and human life. *J. Geophys. Res.*, **114**, G04019, doi:10.1029/2008JG000902.
- Gettelman, A., and Coauthors, 2010: Global simulations of ice nucleation and ice supersaturation with an improved cloud scheme in the Community Atmosphere Model. *J. Geophys. Res.*, **115**, D18216, doi:10.1029/2009JD013797.
- Glisan, J. M., W. J. Gutowski, J. J. Cassano, and M. E. Higgins, 2013: Effects of spectral nudging in WRF on Arctic temperature and precipitation simulations. *J. Climate*, **26**, 3985–3999, doi:10.1175/JCLI-D-12-00318.1.
- Graversen, R. R., and M. Wang, 2009: Polar amplification in a coupled climate model with locked albedo. *Climate Dyn.*, **33**, 629–643, doi:10.1007/s00382-009-0535-6.
- Hines, K. M., and D. H. Bromwich, 2008: Development and testing of Polar Weather Research and Forecasting (WRF) Model. Part I: Greenland Ice Sheet meteorology. *Mon. Wea. Rev.*, **136**, 1971–1989, doi:10.1175/2007MWR2112.1.
- , —, L.-S. Bai, M. Barlage, and A. S. Slater, 2011: Development and testing of Polar Weather Research and Forecasting Model. Part III: Arctic land. *J. Climate*, **24**, 26–48, doi:10.1175/2010JCLI3460.1.
- , —, L. Bai, C. M. Bitz, J. G. Powers, and K. W. Manning, 2015: Sea ice enhancements to Polar WRF. *Mon. Wea. Rev.*, **143**, 2363–2385, doi:10.1175/MWR-D-14-00344.1.

- Hwang, Y.-T., D. M. W. Frierson, and J. E. Kay, 2011: Coupling between Arctic feedbacks and changes in poleward energy transport. *Geophys. Res. Lett.*, **38**, L17704, doi:10.1029/2011GL048546.
- Intrieri, J. M., C. W. Fairall, M. D. Shupe, P. O. G. Persson, E. L. Andreas, P. S. Guest, and R. E. Moritz, 2002: An annual cycle of Arctic surface cloud forcing at SHEBA. *J. Geophys. Res.*, **107**, 8039, doi:10.1029/2000JC000439.
- Jeffries, M. O., and J. Richter-Menge, 2015: The Arctic [in “State of the Climate in 2014”]. *Bull. Amer. Meteor. Soc.*, **96** (7), ES127–ES148, doi:10.1175/BAMS-D-14-00134.1.
- Karlsson, J., and G. Svensson, 2011: The simulation of Arctic clouds and their influence on the winter surface temperature in present-day climate in the CMIP3 multi-model dataset. *Climate Dyn.*, **36**, 623–635, doi:10.1007/s00382-010-0758-6.
- Kay, J. E., and A. Gettelman, 2009: Cloud influence on and response to seasonal Arctic sea ice loss. *J. Geophys. Res.*, **114**, D18204, doi:10.1029/2009JD011773.
- , T. L’Ecuyer, A. Gettelman, G. Stephens, and C. O’Dell, 2008: The contribution of cloud and radiation anomalies to the 2007 Arctic sea ice extent minimum. *Geophys. Res. Lett.*, **35**, L08503, doi:10.1029/2008GL033451.
- Key, J. R., X. Wang, J. C. Stoeve, and C. Fowler, 2001: Estimating the cloudy-sky albedo of sea ice and snow from space. *J. Geophys. Res.*, **106**, 12 489–12 497, doi:10.1029/2001JD900069.
- Klein, S. A., and D. L. Hartmann, 1993: The seasonal cycle of low stratiform clouds. *J. Climate*, **6**, 1587–1606, doi:10.1175/1520-0442(1993)006<1587:TSCOLS>2.0.CO;2.
- , and Coauthors, 2009: Intercomparison of model simulations of mixed-phase clouds observed during the ARM Mixed-Phase Arctic Cloud Experiment: Part I. Single-layer cloud. *Quart. J. Roy. Meteor. Soc.*, **135**, 979–1002, doi:10.1002/qj.416.
- Kupiszewski, P., and Coauthors, 2013: Vertical profiling of aerosol particles and trace gases over the central Arctic Ocean during summer. *Atmos. Chem. Phys.*, **13**, 12 405–12 431, doi:10.5194/acp-13-12405-2013.
- Leck, C., and E. Svensson, 2015: Importance of aerosol composition and mixing state for cloud droplet activation over the Arctic pack ice in summer. *Atmos. Chem. Phys.*, **15**, 2545–2568, doi:10.5194/acp-15-2545-2015.
- Lim, K.-S. S., and S.-Y. Hong, 2010: Development of an effective double-moment cloud microphysics scheme with prognostic cloud condensation nuclei (CCN) for weather and climate models. *Mon. Wea. Rev.*, **138**, 1587–1612, doi:10.1175/2009MWR2968.1.
- Lindsay, R. W., J. Zhang, A. Schweiger, M. Steele, and H. Stern, 2009: Arctic sea ice retreat in 2007 follows thinning trend. *J. Climate*, **22**, 165–176, doi:10.1175/2008JCLI2521.1.
- Liu, X., and Coauthors, 2012: Toward a minimal representation of aerosols in climate models: Description and evaluation in the Community Atmosphere Model CAM5. *Geosci. Model Dev.*, **5**, 709–739, doi:10.5194/gmd-5-709-2012.
- Lobl, E., 2001: Joint Advanced Microwave Scanning Radiometer (AMSR) Science Team meeting. Earth Observer, Vol. 13, No. 13, EOS Project Science Office, Greenbelt, MD, 3–9. [Available online at http://www.acrim.com/Reference%20Files/Earth%20Observer_may_jun01.pdf.]
- Luo, Y., K.-M. Xu, H. Morrison, and G. McFarquhar, 2008: Arctic mixed-phase clouds simulated by a cloud-resolving model: Comparison with ARM observations and sensitivity to microphysics parameterizations. *J. Atmos. Sci.*, **65**, 1285–1303, doi:10.1175/2007JAS2467.1.
- Martin, M., R. Y.-W. Chang, B. Sierau, S. Sjogren, E. Swietlicki, J. P. D. Abbatt, C. Leck, and U. Lohmann, 2011: Cloud condensation nuclei closure study on summertime Arctic aerosol. *Atmos. Chem. Phys.*, **11**, 11 335–11 350, doi:10.5194/acp-11-11335-2011.
- Mauritsen, T., and Coauthors, 2011: An Arctic CCN-limited cloud-aerosol regime. *Atmos. Chem. Phys.*, **11**, 165–173, doi:10.5194/acp-11-165-2011.
- McFarquhar, G. M., and Coauthors, 2011: Indirect and Semi-Direct Aerosol Campaign (ISDAC): The impact of Arctic aerosols on clouds. *Bull. Amer. Meteor. Soc.*, **92**, 183–201, doi:10.1175/2010BAMS2935.1.
- McInnes, K. L., and J. A. Curry, 1995: Modeling the mean and turbulent structure of the summertime Arctic cloudy boundary layer. *Bound.-Layer Meteor.*, **73**, 125–143, doi:10.1007/BF00708933.
- Morrison, H., and A. Gettelman, 2008: A new two-moment bulk stratiform cloud microphysics scheme in the Community Atmosphere Model, version 3 (CAM3). Part I: Description and numerical tests. *J. Climate*, **21**, 3642–3659, doi:10.1175/2008JCLI2105.1.
- , J. A. Curry, and V. I. Khvorostyanov, 2005: A new double-moment microphysics scheme for application in cloud and climate models. Part I: Description. *J. Atmos. Sci.*, **62**, 1665–1677, doi:10.1175/JAS3446.1.
- , J. O. Pinto, J. A. Curry, and G. M. McFarquhar, 2008: Sensitivity of modeled Arctic mixed-phase stratocumulus to cloud condensation and ice nuclei over regionally varying surface conditions. *J. Geophys. Res.*, **113**, D05203, doi:10.1029/2007JD008729.
- , G. Thompson, and V. Tatarskii, 2009: Impact of cloud microphysics on the development of trailing stratiform precipitation in a simulated squall line: Comparison of one- and two-moment schemes. *Mon. Wea. Rev.*, **137**, 991–1007, doi:10.1175/2008MWR2556.1.
- , G. de Boer, G. Feingold, J. Harrington, M. D. Shupe, and K. Sulia, 2012: Resilience of persistent Arctic mixed-phase clouds. *Nat. Geosci.*, **5**, 11–17, doi:10.1038/ngeo1332.
- Nakanishi, M., and H. Niino, 2006: An improved Mellor–Yamada level-3 model: Its numerical stability and application to a regional prediction of advection fog. *Bound.-Layer Meteor.*, **119**, 397–407, doi:10.1007/s10546-005-9030-8.
- Park, S., C. S. Bretherton, and P. J. Rasch, 2014: Integrating cloud processes in the Community Atmosphere Model, version 5. *J. Climate*, **27**, 6821–6856, doi:10.1175/JCLI-D-14-00087.1.
- Perovich, D. K., T. C. Grenfell, B. Light, and P. V. Hobb, 2002: Seasonal evolution of Arctic sea ice albedo. *J. Geophys. Res.*, **107**, 8044, doi:10.1029/2000JC000438.
- Powers, J. G., K. W. Manning, D. H. Bromwich, J. J. Cassano, and A. M. Cayette, 2012: A decade of Antarctic science support through AMPS. *Bull. Amer. Meteor. Soc.*, **93**, 1699–1712, doi:10.1175/BAMS-D-11-00186.1.
- Randall, D., and Coauthors, 1998: Status of and outlook for large-scale modeling of atmosphere–ice–ocean interactions in the Arctic. *Bull. Amer. Meteor. Soc.*, **79**, 197–219, doi:10.1175/1520-0477(1998)079<0197:SOAOFLL>2.0.CO;2.
- Roberts, A., and Coauthors, 2015: Simulating transient ice–ocean Ekman transport in the Regional Arctic System Model and Community Earth System Model. *Ann. Glaciol.*, **56**, doi:10.3189/2015AoG69A760.
- Sedlar, J., and M. D. Shupe, 2014: Characteristic nature of vertical motions observed in Arctic mixed-phase stratocumulus. *Atmos. Chem. Phys.*, **14**, 3461–3478, doi:10.5194/acp-14-3461-2014.
- , and Coauthors, 2011: A transitioning Arctic surface energy budget: The impacts of solar zenith angle, surface albedo and

- cloud radiative forcing. *Climate Dyn.*, **37**, 1643–1660, doi:10.1007/s00382-010-0937-5.
- , M. D. Shupe, and M. Tjernström, 2012: On the relationship between thermodynamic structure and cloud top, and its climate significance in the Arctic. *J. Climate*, **25**, 2374–2393, doi:10.1175/JCLI-D-11-00186.1.
- Serreze, M. C., and J. Francis, 2006: The Arctic amplification debate. *Climatic Change*, **76**, doi:10.1007/s10584-005-9017-y.
- , A. P. Barrett, J. C. Stroeve, D. N. Kindig, and M. M. Holland, 2009: The emergence of surface-based Arctic amplification. *Cryosphere*, **3**, 11–19, doi:10.5194/tc-3-11-2009.
- Shupe, M. D., T. Uttal, and S. Y. Matrosov, 2005: Arctic cloud microphysics retrievals from surface-based remote sensors at SHEBA. *J. Appl. Meteor.*, **44**, 1544–1562, doi:10.1175/JAM2297.1.
- , P. O. G. Persson, I. M. Brooks, M. Tjernström, J. Sedlar, T. Mauritsen, S. Sjogren, and C. Leck, 2013: Cloud and boundary layer interactions over the Arctic sea-ice in late summer. *Atmos. Chem. Phys.*, **13**, 9379–9400, doi:10.5194/acp-13-9379-2013.
- , M. Tjernström, and P. O. G. Persson, 2015: Challenge of Arctic clouds and their implications for surface radiation [in “State of the Climate in 2014”]. *Bull. Amer. Meteor. Soc.*, **96** (7), S130–S131, doi:10.1175/2015BAMSStateoftheClimate.1.
- Skamarock, W. C., and Coauthors, 2008: A description of the Advanced Research WRF version 3. NCAR Tech. Note NCAR/TN-475+STR, 113 pp., doi:10.5065/D68S4MVH.
- Smith, W. L., Jr., and Coauthors, 2017: Arctic Radiation–IceBridge Sea and Ice Experiment (ARISE): The Arctic Radiant Energy System during the critical seasonal ice transition. *Bull. Amer. Meteor. Soc.*, doi:10.1175/BAMS-D-14-00277.1, in press.
- Solomon, A., M. D. Shupe, O. Persson, H. Morrison, T. Yamaguchi, P. M. Caldwell, and G. de Boer, 2014: The sensitivity of springtime Arctic mixed-phase stratocumulus clouds to surface-layer and cloud-top inversion-layer moisture sources. *J. Atmos. Sci.*, **71**, 574–595, doi:10.1175/JAS-D-13-0179.1.
- , G. Feingold, and M. D. Shupe, 2015: The role of ice nuclei recycling in the maintenance of cloud ice in Arctic mixed-phase stratocumulus. *Atmos. Chem. Phys.*, **15**, 10 631–10 643, doi:10.5194/acp-15-10631-2015.
- Sotiropoulou, G., J. Sedlar, M. Tjernström, M. D. Shupe, I. M. Brooks, and P. O. G. Persson, 2014: The thermodynamic structure of summer Arctic stratocumulus and the dynamic coupling to the surface. *Atmos. Chem. Phys.*, **14**, 12 573–12 592, doi:10.5194/acp-14-12573-2014.
- , —, R. Forbes, and M. Tjernström, 2016: Summer Arctic clouds in the ECMWF forecast model: An evaluation of cloud parametrization schemes. *Quart. J. Roy. Meteor. Soc.*, **142**, 387–400, doi:10.1002/qj.2658.
- Steinhoff, D. F., D. H. Bromwich, and A. J. Monaghan, 2013: Dynamics of the foehn mechanism in the McMurdo Dry Valleys of Antarctica from Polar WRF. *Quart. J. Roy. Meteor. Soc.*, **139**, 1615–1631, doi:10.1002/qj.2038.
- Thompson, G., and T. Eidhammer, 2014: A study of aerosol impacts on clouds and precipitation development in a large winter cyclone. *J. Atmos. Sci.*, **71**, 3636–3658, doi:10.1175/JAS-D-13-0305.1.
- Tjernström, M., J. Sedlar, and M. D. Shupe, 2008: How well do regional climate models reproduce radiation and clouds in the Arctic? An evaluation of ARCMIP simulations. *J. Appl. Meteor. Climatol.*, **47**, 2405–2422, doi:10.1175/2008JAMC1845.1.
- , and Coauthors, 2012: Meteorological conditions in the central Arctic during the Arctic Summer Cloud Ocean Study (ASCOS). *Atmos. Chem. Phys.*, **12**, 6863–6889, doi:10.5194/acp-12-6863-2012.
- , and Coauthors, 2014: The Arctic Summer Cloud Ocean Study (ASCOS): Overview and experimental design. *Atmos. Chem. Phys.*, **14**, 2823–2869, doi:10.5194/acp-14-2823-2014.
- Uttal, T., and Coauthors, 2002: The Surface Heat Budget of the Arctic Ocean. *Bull. Amer. Meteor. Soc.*, **83**, 255–275, doi:10.1175/1520-0477(2002)083<0255:SHBOTA>2.3.CO;2.
- Vavrus, S., 2004: The impact of cloud feedbacks on Arctic climate under greenhouse forcing. *J. Climate*, **17**, 603–615, doi:10.1175/1520-0442(2004)017<0603:TIOCFO>2.0.CO;2.
- , D. Waliser, A. Schweiger, and J. Francis, 2009: Simulations of 20th and 21st century Arctic cloud amount in the global climate models assessed in the IPCC AR4. *Climate Dyn.*, **33**, 1099–1115, doi:10.1007/s00382-008-0475-6.
- , U. S. Bhatt, and V. A. Alexeev, 2011: Factors influencing simulated changes in future Arctic cloudiness. *J. Climate*, **24**, 4817–4830, doi:10.1175/2011JCLI4029.1.
- Verlinde, H., and Coauthors, 2007: The Mixed-Phase Arctic Cloud Experiment. *Bull. Amer. Meteor. Soc.*, **88**, 205–221, doi:10.1175/BAMS-88-2-205.
- Wesslén, C., M. Tjernström, D. H. Bromwich, G. de Boer, A. M. L. Ekman, L.-S. Bai, and S.-H. Wang, 2014: The Arctic summer atmosphere: An evaluation of reanalyses using ASCOS data. *Atmos. Chem. Phys.*, **14**, 2605–2624, doi:10.5194/acp-14-2605-2014.
- Westwater, E. R., Y. Han, M. D. Shupe, and S. Y. Matrosov, 2001: Analysis of integrated cloud liquid and precipitable water vapor retrievals from microwave radiometers during Surface Heat Budget of the Arctic Ocean project. *J. Geophys. Res.*, **106**, 32 019–32 030, doi:10.1029/2000JD000055.
- Williams, K., and M. Webb, 2009: A quantitative performance assessment of cloud regimes in climate models. *Climate Dyn.*, **33**, 141–157, doi:10.1007/s00382-008-0443-1.
- Wilson, A. B., D. H. Bromwich, and K. M. Hines, 2011: Evaluation of Polar WRF forecasts on the Arctic System Reanalysis domain: Surface and upper air analysis. *J. Geophys. Res.*, **116**, D11112, doi:10.1029/2010JD015013.
- , —, and —, 2012: Evaluation of Polar WRF forecasts on the Arctic System Reanalysis domain: 2. Atmospheric hydrologic cycle. *J. Geophys. Res.*, **117**, D04107, doi:10.1029/2011JD016765.
- Xu, K.-M., and D. A. Randall, 1996: A semiempirical cloudiness parameterization for use in climate models. *J. Atmos. Sci.*, **53**, 3084–3102, doi:10.1175/1520-0469(1996)053<3084:ASCPFU>2.0.CO;2.